Available online at www.sciencedirect.com
SCIENCE DIRECT®
International Journal of Plasticity 22 (2006) 1799–1824
INTERNATIONAL JOURNAL OF Plasticity
www.elsevier.com/locate/ijplas

Design of microstructure-sensitive properties in elasto-viscoplastic polycrystals using multi-scale homogenization

Veera Sundararaghavan, Nicholas Zabaras *

Materials Process Design and Control Laboratory, Sibley School of Mechanical and Aerospace Engineering, 188 Frank, H.T. Rhodes Hall, Cornell University, Ithaca, NY 14853-3801, USA

Received 23 October 2005; received in final revised form 12 January 2006
Available online 7 March 2006

Abstract

Evolution of properties during processing of materials depends on the underlying material microstructure. A finite element homogenization approach is presented for calculating the evolution of macro-scale properties during processing of microstructures. A mathematically rigorous sensitivity analysis of homogenization is presented that is used to identify optimal forging rates in processes that would lead to a desired microstructure response. Macro-scale parameters such as forging rates are linked with microstructure deformation using boundary conditions drawn from the theory of multi-scale homogenization. Homogenized stresses at the macro-scale are obtained through volume-averaging laws. A constitutive framework for thermo-elastic–viscoplastic response of single crystals is utilized along with a fully-implicit Lagrangian finite element algorithm for modelling microstructure evolution. The continuum sensitivity method (CSM) used for designing processes involves differentiation of the governing field equations of homogenization with respect to the processing parameters and development of the weak forms for the corresponding sensitivity equations that are solved using finite element analysis. The sensitivity of the deformation field within the microstructure is exactly defined and an averaging principle is developed to compute the sensitivity of homogenized stresses at the macro-scale due to perturbations in the process parameters. Computed sensitivities are used within a gradient-based optimization framework for controlling the response of the microstructure. Development of texture and stress–strain response in 2D and 3D FCC aluminum polycrystalline aggregates using the homogenization algorithm is compared with both Taylor-based

* Corresponding author. Tel.: +1 607 255 9104; fax: +1 607 255 1222.
E-mail address: zabaras@cornell.edu (N. Zabaras).
URL: http://mpdc.mae.cornell.edu/ (N. Zabaras).

0749-6419/$ - see front matter
doi:10.1016/j.ijplas.2006.01.001

simulations and published experimental results. Processing parameters that would lead to a desired equivalent stress–strain curve in a sample poly-crystalline microstructure are identified for single and two-stage loading using the design algorithm.

Keywords: Homogenization; Polycrystal plasticity; Microstructure response; Microstructure-sensitive design; Thermomechanical deformation; Sensitivity analysis

1. Introduction

The thermo-mechanical description of polycrystals is usually based on two different scales. The macro-scale is associated with a homogenized continuum and the meso-scale is characterized by the underlying microstructure. For linearly elastic heterogeneous solids, exact averaging theorems and several homogenization models have been developed in Nemat-Nasser and Hori (1993), starting with the pioneering work of Hill (1952, 1965). There are also several contributions to the development of a similar treatment for homogenization of finitely deformed heterogeneous solids (e.g. see Nemat-Nasser, 1999; Hill, 1972, 1984; Havner, 1992).

The emphasis of this paper is on the calculation and design of effective response of a polycrystal microstructure and study of the development of textural features in polycrystalline materials through homogenization. Simulation of texture evolution in polycrystals has been well studied in the past (e.g. for a review see Kocks et al., 1998). Many of the related works apply the Taylor-type micro-macro transition which assumes a purely kinematic constraint mainly that all grains are subjected to the same deformation. This assumption satisfies compatibility but fails to account for equilibrium across grain boundaries. The effect of stereology and formation of disoriented regions within crystals due to non-uniform deformation are not taken into account. In order to model these heterogeneities, several researchers have modelled discretized grain structures (Harren and Asaro, 1989; Bronkhorst et al., 1992; Becker and Panchanadeeswaran, 1995; Beaudoin et al., 1996; Mika and Dawson, 1999) where microstructural constituents are idealized grains with a fixed topology, or realistic polyhedral grains in two or three dimensions (Sarma et al., 2002; Matous and Maniatty, 2004; Diard et al., 2005). In many of these cases, a velocity-based finite element formulation is used (Beaudoin et al., 1996; Sarma et al., 2002; Mika and Dawson, 1999) or displacement-based finite element formulations are used, frequently implemented into commercial finite element codes (Bronkhorst et al., 1992; Becker and Panchanadeeswaran, 1995).

The main feature of the present work is the use of alternative multi-scale transitions that have been proposed using the theory of homogenization based on averaging theorems for linking scales (Nemat-Nasser, 1999). In these models, the Taylor assumption arises naturally as a linking assumption and new linking assumptions that satisfy the basic averaging theorems of Hill (1972) are identified. Such linking procedures for modelling crystal plasticity were originally reported in Miehe et al. (1999) for polycrystalline microstructures. This approach is presently advanced towards interrogation of complex 2D and 3D microstructures using single-crystal constitutive models based on the continuum slip theory (Balasubramanian and Anand, 2002). The polycrystal representative volume element is modelled with a displacement-based fully-implicit updated

Lagrangian finite element formulation in thermo-mechanical loading conditions using multi-scale boundary conditions arising from the theory of large strain homogenization. Mechanical properties are obtained through associated volume-averaging laws. The results of the homogenization scheme are compared with ODF-Taylor, aggregate-Taylor and experimental results based on the development of texture and stress–strain response.

The homogenization procedure is then used to construct a novel optimization scheme for tailoring material response to loading. Very few published works in literature discuss design of processes leading to stipulated material performance requirements (materials by design/microstructure-sensitive design). Significant contributions include (Adams et al., 2001) where the authors discuss the design of a compliant beam so as to maximize the deflection without plastically deforming the beam. Strategies for controlling processes to tailor texture and texture-dependent properties were introduced in Acharjee and Zabaras (2003); Ganapathysubramanian and Zabaras (2004); Sundararaghavan and Zabaras (2005a,b). The emphasis of the present work is on identifying process modes in single- and two-stage processes for controlling the final stress–strain response of poly-crystalline micro-structures. A novel continuum sensitivity method (CSM) is used for designing processes. This involves differentiation of the governing field equations of homogenization with respect to the processing parameters and development of the weak forms for the corresponding sensitivity equations that are solved using finite element analysis. An averaging principle is then developed to compute the sensitivity of the homogenized stresses at the macro-scale due to perturbations in the process parameters. Computed sensitivities are used within a gradient-based optimization framework for controlling the response of the microstructure. The rest of the paper is organized as follows. In Section 2, the microstructure interrogation technique used is introduced followed in Section 3 by a presentation of the continuum sensitivity based process design methodology. In Section 4, we present examples of homogenization and applications to design problems of practical significance. Conclusions are summarized in Section 5.

2. Microstructure interrogation

The approach adopted here for interrogation of microstructures involves finite element based elasto-visco-plastic analysis of microstructures using constitutive models based on the continuum slip theory. The overall response of the microstructure at the macro-scale is derived on the basis of homogenization. In this section, the microstructure interrogation and property evaluation scheme is systematically developed using the theory of non-linear homogenization.

Let $\boldsymbol{y} : \mathscr{B}_{\text{ref}} \rightarrow \mathscr{B}$ represent the non-linear deformation map of the microstructure at time t, and $\boldsymbol{F} = \nabla_{\text{ref}}\boldsymbol{y}$ the associated tangent map (see Fig. 1). $\boldsymbol{F}$ maps points $\boldsymbol{Y} \in \mathscr{B}_{\text{ref}}$ onto points $\boldsymbol{y}(\boldsymbol{Y},t)$ of the current configuration $\mathscr{B}$. The reference microstructure configuration is considered of volume $V(\mathscr{B}_{\text{ref}})$ and boundary $\partial\mathscr{B}_{\text{ref}}$ with outward normal $\boldsymbol{N}$. The microstructure at time t of volume $V(\mathscr{B})$ and boundary $\partial\mathscr{B}$ with outward normal $\boldsymbol{n}$ is attached to the material point $\mathbf{X}$ in the macro-continuum (see Fig. 1). Further, we use superposed bars (e.g. $\bar{\boldsymbol{F}}$) to denote homogenized quantities and angular brackets (e.g. $\langle \boldsymbol{F} \rangle$) to denote volume-averaged quantities. In the subsequent analysis, the standard tensorial notation developed in Gurtin (1981) is followed.

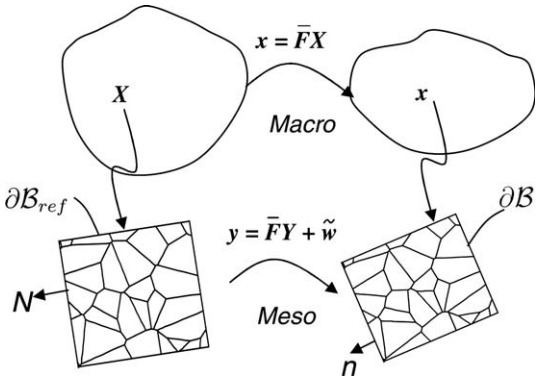

Fig. 1. The microstructure homogenization technique: each integration point in the macro-continuum is associated with an underlying microstructure. The microstructure reference configuration ($\mathscr{B}_{\text{ref}}$) and the mapping to the present microstructure configuration ($\mathscr{B}$) are shown in contrast with the homogenized macro-continuum.

The most general assumption behind homogenization theory is that the deformation gradient as seen at the macro-scale can be represented purely in terms of the motion of the exterior boundary of the microstructure (see Hill, 1972),

$$\bar{\boldsymbol{F}} = \frac{1}{V(\mathscr{B}_{\text{ref}})} \int_{\partial \mathscr{B}_{\text{ref}}} \boldsymbol{y} \otimes \boldsymbol{N} \, \mathrm{d}A. \tag{1}$$

The deformation of the microstructure is then related to the homogenized deformation gradient in the macro-continuum based on the assumption,

$$\mathbf{y} = \bar{\boldsymbol{F}}\mathbf{Y} + \tilde{\mathbf{w}}, \tag{2}$$

where the deformation consists of a homogeneous part $\bar{\boldsymbol{F}}\boldsymbol{Y}$ and an inhomogeneous part $\tilde{\mathbf{w}}$ referred to as the fluctuation field. As a consequence, we have the relationship, $\boldsymbol{F} = \bar{\boldsymbol{F}} + \widetilde{\boldsymbol{F}}$ (with $\widetilde{\boldsymbol{F}} = \nabla\tilde{\mathbf{w}}$) between the microscopic ($\boldsymbol{F}$) and the macroscopic ($\bar{\boldsymbol{F}}$) deformation gradients. From the homogenization law (Eq. (1)) and the decomposition described above, it can be shown that the superposed field $\tilde{\mathbf{w}}$ follows the equation

$$\frac{1}{V(\mathscr{B}_{\text{ref}})} \int_{\partial \mathscr{B}_{\text{ref}}} \tilde{\mathbf{w}} \otimes \boldsymbol{N} \, \mathrm{d}A = 0. \tag{3}$$

The condition is satisfied by the use of any one of the three linking assumptions: (1) $\tilde{\mathbf{w}} = 0$ in $\mathscr{B}_{\text{ref}}$, (2) $\tilde{\mathbf{w}} = 0$ in $\partial\mathscr{B}_{\text{ref}}$, and (3) a periodic boundary condition (refer Miehe et al., 1999) which is not dealt with in the present work. The first two multi-scale boundary conditions are popular in homogenization (i) based on Taylor hypothesis that all crystals deform identically ($\boldsymbol{F} = \bar{\boldsymbol{F}}$) and (ii) homogeneous deformation on the boundaries of the microstructure while allowing for non-uniform deformations within the microstructure. The Taylor hypothesis poses a stringent kinematic constraint on the grains and thus provides a stiff response. In addition, as explained earlier, this assumption fails to model inter- and intra-granular mis-orientation development which is a key feature in polycrystalline materials. The second hypothesis, which allows for homogeneous deformations at the boundary of the microstructure (referred to as the *HB* (homogeneous boundary) condition from here on) and inhomogeneous deformation within grains allowing study of mis-orientation evolution, is adopted in this work.

Macroscopic stress is defined according to a simple virtual work consideration. Here, the variation of the internal work δW_{int} performed by the homogenized PK-I stress tensor $\bar{\boldsymbol{P}}$ at the macroscopic point on arbitrarily virtual displacements of the microstructure $\delta \boldsymbol{y}$ is required to be equal to the work δW_{ext} performed by the external loads on the microstructure. Internal work done by the macroscopic stress can be written as

$$\delta W_{\text{int}} = \int_{\mathscr{B}_{\text{ref}}} \bar{\boldsymbol{P}} \cdot \nabla_{\text{ref}} \delta \boldsymbol{y} \, \mathrm{d}V \tag{4}$$

$$= \bar{\boldsymbol{P}} \cdot \int_{\partial \mathscr{B}_{\text{ref}}} \delta \boldsymbol{y} \otimes \boldsymbol{N} \, \mathrm{d}A. \tag{5}$$

External work is given as $\delta W_{\text{ext}} = \int_{\partial \mathscr{B}_{\text{ref}}} \boldsymbol{p} \cdot \delta \boldsymbol{y} \, \mathrm{d}A$, where $\boldsymbol{p}$ is the traction vector at the boundary of the reference microstructure. For the HB condition, the virtual displacements at the boundary of the microstructure are obtained from the variation of the macroscopic deformation gradient as,

$$\delta \boldsymbol{y} = \delta \bar{\boldsymbol{F}} \boldsymbol{Y} \ . \tag{6}$$

Thus, the external work can be written as $\delta W_{\text{ext}} = \delta \bar{\boldsymbol{F}} \cdot \int_{\partial \mathscr{B}_{\text{ref}}} \boldsymbol{Y} \otimes \boldsymbol{p} \, \mathrm{d}A$. For satisfying the balance of virtual work,

$$\delta \bar{\boldsymbol{F}} \cdot \int_{\partial \mathscr{B}_{\text{ref}}} \boldsymbol{Y} \otimes \boldsymbol{p} dA = \bar{\boldsymbol{P}} \cdot \int_{\partial \mathscr{B}_{\text{ref}}} \delta \boldsymbol{y} \otimes \boldsymbol{N} \, \mathrm{d}A = \bar{\boldsymbol{P}} \delta \bar{\boldsymbol{F}} \cdot \int_{\partial \mathscr{B}_{\text{ref}}} \boldsymbol{Y} \otimes \boldsymbol{N} \, \mathrm{d}A = \delta \bar{\boldsymbol{F}} \cdot \bar{\boldsymbol{P}} V(\mathscr{B}_{\text{ref}}).$$

Taking into account the fact that the equality should be satisfied for any arbitrary variation of the deformation gradient tensor $\delta \bar{\boldsymbol{F}}$, we obtain the macroscopic stresses to be of the form

$$\bar{\boldsymbol{P}} = \frac{1}{V(\mathscr{B}_{\text{ref}})} \int_{\partial \mathscr{B}_{\text{ref}}} \boldsymbol{Y} \otimes \boldsymbol{p} \, \mathrm{d}A. \tag{7}$$

An equilibrium state of the micro-structure at a certain stage of the deformation process is then assumed with the equations,

$$\nabla_{\text{ref}} \cdot \boldsymbol{P} = 0 \quad \text{in } \mathscr{B}_{\text{ref}}, \tag{8}$$

$$\boldsymbol{P}^{\text{T}} \boldsymbol{N} = \boldsymbol{p} \quad \text{on } \partial \mathscr{B}_{\text{ref}}. \tag{9}$$

Using the divergence theorem, macroscopic stresses as defined by Eq. (7) can be shown to be the volume-average of the microscopic stresses ($\boldsymbol{P}$)

$$\bar{\boldsymbol{P}} = \frac{1}{V(\mathscr{B}_{\text{ref}})} \int_{\mathscr{B}_{\text{ref}}} \boldsymbol{P} \, \mathrm{d}V = \langle \boldsymbol{P} \rangle. \tag{10}$$

The following relationship between the homogenized PK-1 stress and homogenized Cauchy stress is then assumed

$$\bar{\boldsymbol{P}} = (\det \bar{\boldsymbol{F}}) \bar{\boldsymbol{T}} \bar{\boldsymbol{F}}^{-\text{T}}. \tag{11}$$

Readers are referred to the fact that virtual work principle similar to that used in the derivation of homogenized PK-1 stress can be used to prove that the macroscopic Cauchy stress ($\bar{\boldsymbol{T}}$) is also a volume-average (in the current configuration) of the microstructural counterpart ($\boldsymbol{T}$) as,

$$\bar{\boldsymbol{T}} = \langle \boldsymbol{T} \rangle. \tag{12}$$

However, once Eq. (10) is assumed, then Eq. (11) is used to define the homogenized Cauchy stress. Thus, in the present approach, Eq. (12) is abandoned in favor of Eq. (10) (refer Nemat-Nasser, 1999). It is to be noted that Hill (1984) and Nemat-Nasser (1999) advocate the nominal stress tensor ($\boldsymbol{S} = (\det \boldsymbol{F})\boldsymbol{F}^{-1}\boldsymbol{T}$) as the averaging measure. The choice of PK-I stress as the stress measure for averaging in our work (as also in Miehe et al. (1999)) is motivated by the fact that $\boldsymbol{P}$ and $\boldsymbol{F}$ are work conjugated.

Apart from these definitions, in macro-problems with temperature effects, the temperature linking is achieved through equating the macro- ($\bar{\theta}$) and micro- (θ) temperatures and the macro- and micro-mechanical dissipation. Microstructure (material point) simulations are deemed isothermal in this work since the macro-scale temperature evolution problem is not solved.

The kinematic problem for microstructure deformation employs the updated Lagrangian framework. Here, the total micro-scale deformation gradient $\boldsymbol{F}_{n+1}$ at time $t = t_{n+1}$ of configuration $\mathscr{B}_{n+1}$ with respect to the initial undeformed configuration ($\mathscr{B}_0$) at time $t = 0$ is assumed to be decomposed as

$$\boldsymbol{F}_{n+1} = \nabla_0 \tilde{\boldsymbol{y}}(\boldsymbol{Y}_0, t_{n+1}) = \nabla_n \hat{\boldsymbol{y}}(\boldsymbol{Y}_n, t)\nabla_0 \tilde{\boldsymbol{y}}(\boldsymbol{Y}_0, t_n) = \boldsymbol{F}_{\mathrm{r}}\boldsymbol{F}_n = \boldsymbol{F}^{\mathrm{e}}\boldsymbol{F}^{\mathrm{p}}, \tag{13}$$

where $\boldsymbol{F}^{\mathrm{e}}$ is the micro-scale elastic deformation gradient at time $n+1$, $\boldsymbol{F}^{\mathrm{p}}$ is the micro-scale plastic deformation gradient at time $n+1$, $\boldsymbol{F}_{\mathrm{r}}$ is the relative deformation gradient with respect to the configuration at time n and $\boldsymbol{F}_n$ refers to the total micro-scale deformation gradient in the reference configuration ($\mathscr{B}_n$) with respect to the initial undeformed configuration. Going back to Fig.1, using the updated Lagrangian description of kinematics, $\mathscr{B}_{\mathrm{ref}}$ would now refer to $\mathscr{B}_n$. Quantities used in the derivation of homogenized stresses would now be defined with respect to $\mathscr{B}_n$. For example, the microscopic deformation gradient $\boldsymbol{F}$ would be equal to $\boldsymbol{F}_{\mathrm{r}}$ as defined in Eq. (13).

The equilibrium equations can be expressed in the reference configuration $\mathscr{B}_n$ as,

$$\nabla_n \cdot \boldsymbol{P}_{\mathrm{r}} = \boldsymbol{0}, \tag{14}$$

where the PK-I stress $\boldsymbol{P}_{\mathrm{r}}(\boldsymbol{Y}_n, t)$ is expressed as $\boldsymbol{P}_{\mathrm{r}}(\boldsymbol{Y}_n, t) = (\det \boldsymbol{F}_{\mathrm{r}})\boldsymbol{T}\boldsymbol{F}_r^{-\mathrm{T}}$. The solution of a generic loading increment involves the solution to the principle of virtual work (PVW) given as follows: Calculate $\boldsymbol{y}(\boldsymbol{Y}_n, t)$ such that

$$\int_{\mathscr{B}_n} \boldsymbol{P}_{\mathrm{r}} \cdot \nabla_n \tilde{\boldsymbol{u}} \, \mathrm{d}V_n = 0 \tag{15}$$

for every admissible test function $\tilde{\boldsymbol{u}}$ expressed over the reference configuration $\mathscr{B}_n$. The weak form is solved in an incremental-iterative manner as a result of material non-linearities. FEM is used for the solution of the weak form and bilinear quadrilateral elements are used for the microstructure along with the assumed strain analysis scheme to counter the effect of near-incompressibility. Microstructure homogenization and multi-scaling procedure has been implemented in an object-oriented and parallel environment in C++ and PetSc parallel toolbox and is applicable to both 2D and 3D microstructures, building from our earlier work on large deformation process modeling and design in Akkaram and Zabaras (2001). The microstructure material point problem has been parallelized by efficiently partitioning microstructure elements to every processor. Microstructure interrogation can be thought of as a material point simulator with the macro-point under consideration being subject to deformations corresponding to various processing conditions that are transferred to the boundaries of the microstructure using the HB condition.

In this work, the equivalent strain is computed based on the volume-average of the deformation rate ($\bar{\boldsymbol{D}} = \langle \boldsymbol{D} \rangle$) following the measure for which the constitutive laws in Balasubramanian and Anand (2002) were originally developed. This is performed as a post processing step and is not required for multi-scaling. The average effective plastic strain $\bar{\epsilon}_{\text{eff}}$ is defined as

$$\bar{\epsilon}_{\text{eff}} = \int_0^t \sqrt{\frac{2}{3}\bar{\boldsymbol{D}} \cdot \bar{\boldsymbol{D}}}\, \mathrm{d}t. \tag{16}$$

Average strain measures can be alternatively derived (van der Sluis et al., 2000) through an additional assumption that the macroscopic plastic work rate equals the plastic work rate of the microstructure in an averaged sense (Gurson, 1977). It should be noted that this assumption does not hold for the definition of average deformation rate used in this work.

The equivalent stress for the microstructure is represented using the von-Mises norm as

$$\bar{\sigma}_{\text{eff}} = \sqrt{\frac{3}{2}\bar{\boldsymbol{T}}'.\bar{\boldsymbol{T}}'}. \tag{17}$$

2.1. Single crystal constitutive problem

The constitutive problem adopted for a single FCC crystal $\boldsymbol{T} = \boldsymbol{T}(\boldsymbol{F}_{n+1}, \theta, \text{state})$, and computation of reorientations of crystals is described in detail in Balasubramanian and Anand (2002). Useful features of this model include its ability to accurately model large strain elasto-viscoplastic response incorporating strain rate and temperature effects. A fully-implicit integration scheme with implicit evaluation of consistent tangent moduli as proposed in Ganapathysubramanian and Zabaras (2005) is used in the microstructure deformation simulation. The constitutive problem uses a total-Lagrangian description of deformation gradient (with $\boldsymbol{F}_{n+1}$ denoting the deformation gradient at current time with respect to the initial undeformed configuration).

In the constitutive model, it is assumed that deformation takes place in a single crystal through dislocation glide and the evolution of the plastic flow is given by

$$\dot{\boldsymbol{F}}^{\text{p}}(\boldsymbol{F}^{\text{p}})^{-1} = \boldsymbol{L} = \sum_{\alpha} \dot{\gamma}^{\alpha} \boldsymbol{S}_0^{\alpha}, \tag{18}$$

where $\boldsymbol{S}_0^{\alpha} = \boldsymbol{m}^{\alpha} \otimes \boldsymbol{n}^{\alpha}$ is the Schmid tensor, $\dot{\gamma}^{\alpha}$ is the plastic shearing rate on the slip system α and $\boldsymbol{m}^{\alpha}$ and $\boldsymbol{n}^{\alpha}$ are the slip directions and the slip plane normals, respectively, in the initial configuration (at $t = 0$). An Euler-backward time integration procedure leads to the following approximation:

$$\boldsymbol{F}^{\text{p}} = \exp\left(\Delta t \sum_{\alpha} \dot{\gamma}^{\alpha} \boldsymbol{S}_0^{\alpha}\right) \boldsymbol{F}_n^{\text{p}} \approx \left(\boldsymbol{I} + \Delta t \sum_{\alpha} \dot{\gamma}^{\alpha} \boldsymbol{S}_0^{\alpha}\right) \boldsymbol{F}_n^{\text{p}} \tag{19}$$

for small Δt. Substituting Eq. (19) into Eq. (13) results in:

$$\boldsymbol{F}^{\text{e}} = \boldsymbol{F}_{\text{trial}}^{\text{e}} \left(\boldsymbol{I} - \Delta t \sum_{\alpha} \dot{\gamma}^{\alpha} \boldsymbol{S}_0^{\alpha}\right), \tag{20}$$

where $\boldsymbol{F}_{\text{trial}}^{\text{e}}$ is the trial elastic deformation gradient and is given as $\boldsymbol{F}_{n+1}(\boldsymbol{F}_n^{\text{p}})^{-1}$. In the constitutive equations to be defined below, the Green elastic strain measure defined on

the relaxed configuration (plastically deformed, unstressed configuration) $\check{\mathscr{B}}$ is utilized. It is computed using Eq. (20) as

$$\check{\boldsymbol{E}}^{\mathrm{e}} = \frac{1}{2}\left(\boldsymbol{F}^{\mathrm{e}\mathrm{T}}\boldsymbol{F}^{\mathrm{e}} - \boldsymbol{I}\right) = \check{\boldsymbol{E}}^{\mathrm{e}}_{\mathrm{trial}} - \frac{\Delta t}{2}\sum_{\alpha}\dot{\gamma}^{\alpha}\left((\boldsymbol{S}_0^{\alpha})^{\mathrm{T}}(\boldsymbol{F}^{\mathrm{e}}_{\mathrm{trial}})^{\mathrm{T}}\boldsymbol{F}^{\mathrm{e}}_{\mathrm{trial}} + (\boldsymbol{F}^{\mathrm{e}}_{\mathrm{trial}})^{\mathrm{T}}\boldsymbol{F}^{\mathrm{e}}_{\mathrm{trial}}\boldsymbol{S}_0^{\alpha}\right), \tag{21}$$

where $\check{\boldsymbol{E}}^{\mathrm{e}}_{\mathrm{trial}} = \frac{1}{2}((\boldsymbol{F}^{\mathrm{e}}_{\mathrm{trial}})^{\mathrm{T}}\boldsymbol{F}^{\mathrm{e}}_{\mathrm{trial}} - \boldsymbol{I})$.

The conjugate stress measure is then defined as

$$\check{\boldsymbol{T}} = \det\boldsymbol{F}^{\mathrm{e}}(\boldsymbol{F}^{\mathrm{e}})^{-1}\boldsymbol{T}(\boldsymbol{F}^{\mathrm{e}})^{-\mathrm{T}}, \tag{22}$$

where $\boldsymbol{T}$ is the Cauchy stress for the crystal in the sample reference frame. All vector and tensorial quantities are expressed in the initial configuration $\mathscr{B}_0$. Furthermore, crystal specific properties like the stiffness and compliance have to be transformed to this sample reference frame using the crystal orientation ($\boldsymbol{r}$). The constitutive relation, for stress, for small temperature changes about the initial temperature, θ_0, is given by

$$\check{\boldsymbol{T}} = \mathscr{L}^{\mathrm{e}}[\check{\boldsymbol{E}}^{\mathrm{e}} - \boldsymbol{A}(\theta - \theta_0)], \tag{23}$$

where $\mathscr{L}^{\mathrm{e}}$ is the fourth-order anisotropic elasticity tensor expressed in terms of the crystal stiffness parameters and the orientation $\boldsymbol{r}$, and $\boldsymbol{A}$ is the second-order anisotropic thermal expansion tensor. Substitution of Eq. (21) into Eq. (23) results in the following

$$\check{\boldsymbol{T}} = \check{\boldsymbol{T}}_{\mathrm{trial}} - \frac{\Delta t}{2}\sum_{\beta}\dot{\gamma}^{\beta}\mathscr{L}^{\mathrm{e}}\left[(\boldsymbol{S}_0^{\beta})^{\mathrm{T}}(\boldsymbol{F}^{\mathrm{e}}_{\mathrm{trial}})^{T}\boldsymbol{F}^{\mathrm{e}}_{\mathrm{trial}} + (\boldsymbol{F}^{\mathrm{e}}_{\mathrm{trial}})^{T}\boldsymbol{F}^{\mathrm{e}}_{\mathrm{trial}}\boldsymbol{S}_0^{\beta}\right] - (\theta - \theta_0)\mathscr{L}^{\mathrm{e}}[\boldsymbol{A}], \tag{24}$$

where $\check{\boldsymbol{T}}_{\mathrm{trial}} = \mathscr{L}^{\mathrm{e}}[\check{\boldsymbol{E}}^{\mathrm{e}}_{\mathrm{trial}}]$.

Further, if $s^{\alpha}(\theta)$ is the slip system resistance at temperature θ K, then the thermal and athermal components of the slip system resistance and the resolved shear stress are defined as

$$s^{\alpha} = s^{\alpha}_{\mathrm{at}} + s^{\alpha}_{\mathrm{t}}, \tag{25}$$

$$\tau^{\alpha}_{\mathrm{t}} = |\tau^{\alpha}| - s^{\alpha}_{\mathrm{at}}, \tag{26}$$

where the subscripts t and at denote the thermal and athermal parts, respectively, and τ^{α}, the resolved shear stress for the αth slip system, is computed as $\check{\boldsymbol{T}} \bullet \boldsymbol{S}_0^{\alpha}$. Such a formulation was developed in Kothari and Anand (1998) and Balasubramanian and Anand (2002). Here, part of the resolved shear stress has to overcome the athermal barriers (such as strong precipitates). Thermal barriers (such as Peierls stress and forest dislocations) are overcome by a combination of thermal energy and the resolved shear stress. Stress levels with resolved shear stress ($|\tau^{\alpha}|$) greater than slip resistance (s^{α}) are unattainable. If the resolved shear stress exceeds the athermal resistance, slip is activated. The shearing rate is then expressed accordingly as,

$$\dot{\gamma}^{\alpha} = \begin{cases} 0, & \tau^{\alpha}_{\mathrm{t}} \leqslant 0, \\ \dot{\gamma}^{0}\exp\left\{-\frac{\Delta G^{\alpha}(\tau^{\alpha}_{\mathrm{t}}, s^{\alpha}_{\mathrm{t}})}{k_{\mathrm{B}}\theta}\right\}\mathrm{sign}(\tau^{\alpha}), & 0 < \tau^{\alpha}_{\mathrm{t}} < s^{\alpha}_{\mathrm{t}}, \end{cases} \tag{27}$$

where the activation enthalpy is given by

$$\Delta G^{\alpha}(\tau^{\alpha}_{\mathrm{t}}, s^{\alpha}_{\mathrm{t}}) = \Delta F^{\alpha}\left[1 - \left\{\frac{\tau^{\alpha}_{\mathrm{t}}}{s^{\alpha}_{\mathrm{t}}}\right\}^{p}\right]^{q}. \tag{28}$$

In the equation above, ΔF^{α} is the activation energy at $0K$, p and q are material parameters (generally, $0 < p < 1$ and $1 < q < 2$) and k_B is the Boltzmann constant. Furthermore, the slip system resistance parameters s^{α}_{at} and s^{α}_{t} evolve with deformation as

$$\dot{s}^{\alpha} = \sum_{\beta} h^{\alpha\beta} |\dot{\gamma}^{\beta}| \tag{29}$$

and $h^{\alpha\beta}$ is defined as

$$h^{\alpha\beta} = q^{\alpha\beta} h^{\beta} \quad \text{(no sum on } \beta\text{)}, \tag{30}$$

$$h^{\beta} = h^{\beta}_{0} |1 - s^{\beta}/s^{\beta}_{s}|^{r_1} \operatorname{sign}\left\{1 - \frac{s^{\beta}}{s^{\beta}_{s}}\right\}. \tag{31}$$

In Eq. (30), $q^{\alpha\beta}$ represents the latent-hardening parameter with the following property

$$q^{\alpha\beta} = \begin{cases} 1 & \text{if } \alpha = \beta, \\ q_h = 1.4 & \text{if } \alpha \neq \beta. \end{cases} \tag{32}$$

Further, s^{β}_{s} represents the saturation value of s^{β}, h^{β}_{0} and r_1 are material response parameters. For FCC materials, s^{β}_{s}, the saturation state of s^{β}, is considered as a constant in this work. Interested readers are referred to Balasubramanian and Anand (2002) and references therein for a more detailed physical interpretation of parameters in the constitutive model.

An Euler-backward time integration of Eq. (29) along with Eqs. (30) and (31) results in the following

$$s^{\alpha}_{n+1} = s^{\alpha}_{n} + \Delta t \sum_{\beta} q^{\alpha\beta} g^{\beta}(\tau^{\beta}_{n+1}, s^{\beta}_{n+1}, \theta), \tag{33}$$

where $g^{\beta} = h^{\beta}|\dot{\gamma}^{\beta}|$. For FCC materials, the ratio $\eta = \frac{s^{\alpha}_{t}}{s^{\alpha}_{at}}$, which is a constant, is utilized to evaluate the thermal and athermal parts of slip system hardness as

$$s^{\alpha}_{at} = s^{\alpha}_{n+1} \frac{1}{1+\eta}, \tag{34}$$

$$s^{\alpha}_{t} = s^{\alpha}_{n+1} \frac{\eta}{1+\eta}. \tag{35}$$

The resolved shear stress τ^{α} and the slip system resistance s^{α} is solved from the coupled system given by Eqs. (24), (27) and (33) using an iterative scheme (algorithm can be found in Ganapathysubramanian and Zabaras (2005)).

For calculation of texture, we employ the Rodrigues–Frank space representation of texture. Details of neo-Eulerian representations and the use of Rodrigues–Frank space can be found in Ganapathysubramanian and Zabaras (2005). The re-orientation velocity is here evaluated as:

$$\boldsymbol{v} = \frac{\partial \boldsymbol{r}}{\partial t} = \frac{1}{2}(\boldsymbol{\omega} + (\boldsymbol{\omega} \cdot \boldsymbol{r})\boldsymbol{r} + \boldsymbol{\omega} \times \boldsymbol{r}), \tag{36}$$

where $\boldsymbol{r}$ is the orientation (Rodrigues' parametrization) and $\boldsymbol{\omega}$ represents the spin vector defined as $\boldsymbol{\omega} = \operatorname{vect}(\dot{\boldsymbol{R}}^{e}\boldsymbol{R}^{eT}) = \operatorname{vect}(\boldsymbol{\Omega})$, where $\boldsymbol{R}^{e}$ is evaluated through the polar decomposition of the elastic deformation gradient $\boldsymbol{F}^{e}$ as $\boldsymbol{F}^{e} = \boldsymbol{R}^{e}\boldsymbol{U}^{e}$. Considering the Euler-backward time integration of $\dot{\boldsymbol{R}}^{e}\boldsymbol{R}^{eT} = \boldsymbol{\Omega}$, where $\boldsymbol{\Omega}$ is the spin tensor, leads to the following:

$$\boldsymbol{R}^{\mathrm{e}}_{n+1} = \exp(\Delta t \boldsymbol{\Omega}_{n+1}) \boldsymbol{R}^{\mathrm{e}}_{n} \tag{37}$$

and

$$\boldsymbol{\Omega}_{n+1} = \frac{1}{\Delta t} \ln \left\{ \boldsymbol{R}^{\mathrm{e}}_{n+1} \boldsymbol{R}^{\mathrm{e}\mathrm{T}}_{n} \right\}. \tag{38}$$

Once the constitutive problem is solved, $\boldsymbol{F}^{\mathrm{e}}_{n+1}$ can be evaluated from Eq. (20). From the elastic deformation gradient, $\boldsymbol{R}^{\mathrm{e}}_{n+1}$ and $\boldsymbol{R}^{\mathrm{e}}_{n}$ are evaluated and one can then evaluate the spin tensor $\boldsymbol{\Omega}_{n+1}$ using Eq. (38). The re-orientation velocity can be computed from Eq. (36) which is used to update the orientation of the crystal $\boldsymbol{r}$.

This completes the constitutive problem which is solved at each integration point of the discretized microstructure. In addition, to solve the non-linear Eq. (15) for the microstructure, a Newton–Raphson (NR) iterative scheme along with a line search procedure is employed. An implicit technique for linearization of the PK-I stress for the NR iterations based on the constitutive problem described here can be found in Ganapathysubramanian and Zabaras (2005).

Although FE homogenization provides an improved model accounting for non-uniform deformations within the microstructure, two shortcomings need to be pointed out in the context of multi-scaling. Firstly, the dimensions of the microstructure representative volume element (RVE) do not influence the averaging procedure. This arises from the assumption that the microstructure is infinitesimal compared to the macro-scale and hence, is seen as a macroscopic material point. Thus, the homogenization result is independent of the overall dimensions of the microstructure. Secondly, use of first-order expansion of microstructural deformation (Eq. (2)) restricts the analysis to simple deformation modes (rotation, tension, shear or combinations thereof) at the micro-scale. In spite of these drawbacks, the homogenization approach followed here allows additional convenience of using the same algorithm as a plug-in in large strain continuum scale simulations with minimal modifications to account for microstructural degrees of freedom.

3. Continuum sensitivity technique for process optimization at a material point

A problem of interest to manufacturing engineers is to identify improved processing parameters that would closely achieve desired properties in materials. We define the design problem of interest as identification of the right combination of process modes involving plane strain tension/compression (rolling), shear and rotation, and the corresponding process parameters $\boldsymbol{\alpha}$ that would lead to a desired property χ that is a function of the given microstructure. The macro-velocity gradient ($\widetilde{\boldsymbol{L}} = \dot{\bar{\boldsymbol{F}}} \bar{\boldsymbol{F}}^{-1}$) is decomposed uniquely for 2D microstructure analysis as follows:

$$\widetilde{\boldsymbol{L}} = \alpha_1 \begin{bmatrix} 1 & 0 & 0 \\ 0 & -1 & 0 \\ 0 & 0 & 0 \end{bmatrix} + \alpha_2 \begin{bmatrix} 0 & 1 & 0 \\ 1 & 0 & 0 \\ 0 & 0 & 0 \end{bmatrix} + \alpha_3 \begin{bmatrix} 0 & -1 & 0 \\ 1 & 0 & 0 \\ 0 & 0 & 0 \end{bmatrix}. \tag{39}$$

Similar decomposition for 3D deformation problems can be found in Ganapathysubramanian and Zabaras (2004). Each matrix in the decomposition of Eq. (39) corresponds to a given deformation process namely plane strain tension/compression (α_1), plane shear mode (α_2) and rotation mode (α_3). Note that here $\widetilde{\boldsymbol{L}}$ is introduced to define the deformation modes at the macro-scale as in our earlier work and that $\widetilde{\boldsymbol{L}} \neq \bar{\boldsymbol{L}}$.

The macroscopic deformation gradient at time step $n+1$ ($\bar{\boldsymbol{F}}_{n+1}$) is computed based from the definition of $\widetilde{\boldsymbol{L}}_{n+1}$ using a backward Euler approximation as,

$$\bar{\boldsymbol{F}}_{n+1} = \bar{\boldsymbol{F}}_n(\boldsymbol{I} + \widetilde{\boldsymbol{L}}_{n+1}\Delta t). \tag{40}$$

The design problem is posed as the identification of process parameters $\boldsymbol{\alpha} = [\alpha_1, \alpha_2, \alpha_3]$ that would lead to a desired homogenized property χ. This can be stated by the minimization problem:

$$\min_{\boldsymbol{\alpha}} \mathscr{F}(\boldsymbol{\alpha}) = \frac{1}{N_s}\sum_{i=1}^{N_s}(\chi^i(\mathscr{B}(\boldsymbol{\alpha})) - \chi^{\text{desired}^i})^2, \tag{41}$$

where N_s is the total number of sampling points and χ^{desired} is the discrete representation of the desired homogenized microstructural property.

We denote the sensitivity (directional-derivative) of the microstructure to a small change in the process parameter ($\boldsymbol{\alpha}$) as $\overset{\circ}{\mathscr{B}} = \overset{\circ}{\mathscr{B}}(r, t; \boldsymbol{\alpha}, \Delta\boldsymbol{\alpha})$. The ith sensitivity problem is driven by $\Delta\alpha_i = 10^{-5}$ with $\Delta\alpha_j = 0$ for $j \neq i$. The gradients of property (χ) with respect to α_i is calculated as

$$\frac{\partial\chi}{\partial\alpha_i} = \frac{\overset{\circ}{\chi}(\mathbf{r}, t, \alpha_1, \ldots, \alpha_3, 0, \ldots, \Delta\alpha_i, \ldots, 0)}{\Delta\alpha_i}. \tag{42}$$

In general, the homogenized property (χ) is a function of a homogenized field ($\bar{\boldsymbol{\Upsilon}}$). In Examples 4 and 5 of Section 4, the property to be optimized is taken to be the time history of homogenized equivalent stress ($\chi = \bar{\sigma}_{\text{eff}}$). Calculation of the homogenized equivalent stress involves calculation of the sensitivity of the PK-1 stress (in this case, $\boldsymbol{\Upsilon} = \boldsymbol{P}$). The expression for the sensitivity of a homogenized field ($\bar{\boldsymbol{\Upsilon}}$) over the microstructure configuration ($\mathscr{B}$) is determined as follows:

$$\begin{aligned}\overline{\overset{\circ}{\boldsymbol{\Upsilon}}} &= \frac{1}{V(\mathscr{B})}\int_{\mathscr{B}} \overset{\circ}{\boldsymbol{\Upsilon}}(\boldsymbol{y}, t; \boldsymbol{\alpha})\,\mathrm{d}V \\ &= -\frac{\overset{\circ}{V}(\mathscr{B})}{V(\mathscr{B})}\bar{\boldsymbol{\Upsilon}} + \frac{1}{V(\mathscr{B})}\int_{\mathscr{B}}\left(\overset{\circ}{\Upsilon}(\boldsymbol{y}, t; \boldsymbol{\alpha}) + \Upsilon(\boldsymbol{y}, t; \boldsymbol{\alpha})\mathrm{tr}\left(\overset{\circ}{\boldsymbol{F}}_{n+1}\boldsymbol{F}_{n+1}^{-1}\right)\right)\mathrm{d}V\end{aligned} \tag{43}$$

Sensitivities of the homogenized property are then used in the steepest descent optimization algorithm to obtain the optimum process parameters that minimize the objective function in Eq. (41). Computational schemes for rigorously computing these sensitivities from the governing equations of microstructure evolution are described next.

3.1. Deformation sensitivity problem

The interest in this problem is to compute how perturbations on the macro-design variables $\boldsymbol{\alpha}$ affect the micro-fields – mainly the stresses within the microstructure. We compute the resulting variation of the microstructure and other microstructural properties from the perturbation $\overset{\circ}{\bar{\boldsymbol{F}}}_{n+1}$ of $\bar{\boldsymbol{F}}_{n+1}$. $\overset{\circ}{\bar{\boldsymbol{F}}}_{n+1}$ is in turn obtained from perturbation $\overset{\circ}{\widetilde{\boldsymbol{L}}}_{n+1}$ of the macro-velocity gradient $\widetilde{\boldsymbol{L}}_{n+1}$ as

$$\overset{\circ}{\bar{\boldsymbol{F}}}_{n+1} = (\boldsymbol{I} + \widetilde{\boldsymbol{L}}_{n+1}\Delta t)(\overset{\circ}{\bar{\boldsymbol{F}}}_n + \overset{\circ}{\widetilde{\boldsymbol{L}}}_{n+1}\bar{\boldsymbol{F}}_{n+1}\Delta t). \tag{44}$$

Similar multi-scale boundary conditions such as those developed in the previous section can be used for the sensitivity problem. In particular, we define the sensitivity linking as follows: the sensitivity of the averaged deformation gradient at a material point is taken to be the same as the sensitivity of the deformation gradient on the boundary of the underlying microstructure, in the reference frame. The equilibrium equation for the microstructure is then considered and design-differentiated. This differential, sensitivity equilibrium equation is posed in a weak form so as to establish a principle of virtual work like equation for the calculation of the sensitivity of deformation fields in the microstructure. Consistent with this mode of analysis, the sensitivity constitutive problem is directly derived by differentiating the constitutive equations given in the previous section. Described below is the analysis for the development of a total Lagrangian sensitivity formulation for the kinematic problem (with microstructure at time step $t = t_0$ as the reference configuration at time step n). The design-differentiation of the equilibrium equation (Eq. (14)) results in:

$$\overset{\circ}{\overbrace{\nabla_{0\bullet}\boldsymbol{P}}} = \boldsymbol{0}, \tag{45}$$

where $\boldsymbol{P}$ is the PK-I stress defined earlier. A variational form for the sensitivity equilibrium equation (for parameter sensitivity) can be posed as follows: Evaluate $\overset{\circ}{\boldsymbol{y}} = \overset{\circ}{\boldsymbol{y}}(\boldsymbol{Y}_0, t; \boldsymbol{\alpha}, \Delta\boldsymbol{\alpha})$ such that

$$\int_{\mathscr{B}_0} \overset{\circ}{\boldsymbol{P}} \bullet \nabla_0 \tilde{\boldsymbol{\eta}} \, \mathrm{d}V_0 = 0 \tag{46}$$

for every $\tilde{\boldsymbol{\eta}}$, a kinematically admissible sensitivity deformation field expressed over the reference configuration. In order to solve the weak form, defined by Eq. (46), relationships between (a) $\overset{\circ}{\boldsymbol{F}}_{n+1}$ and $\overset{\circ}{\boldsymbol{y}}$ (sensitivity of the kinematic problem) and (b) $\overset{\circ}{\boldsymbol{P}}$ and $[\overset{\circ}{\boldsymbol{F}}_{n+1}, \overset{\circ}{\theta}]$ (sensitivity of the constitutive problem) needs to be defined. The relationship between $\overset{\circ}{\boldsymbol{F}}_{n+1}$ and $\overset{\circ}{\boldsymbol{y}}$ is purely kinematic ($\overset{\circ}{\boldsymbol{F}}_{n+1} = \nabla_0 \overset{\circ}{\boldsymbol{y}}$). The relationship between $\overset{\circ}{\boldsymbol{P}}$ and $[\overset{\circ}{\boldsymbol{F}}_{n+1}, \overset{\circ}{\theta}]$ is obtained from the sensitivity constitutive problem to be discussed in Section 3.2 and takes the form:

$$\overset{\circ}{\boldsymbol{P}} = \mathscr{B}[\overset{\circ}{\boldsymbol{F}}_{n+1}] + \boldsymbol{A}\overset{\circ}{\theta} + \boldsymbol{B}, \tag{47}$$

where $\mathscr{B}$ is a fourth order tensor and $\boldsymbol{A}$, $\boldsymbol{B}$ are second order tensors. These tensors, are constants, defined from known direct and sensitivity fields at the previous time step, are obtained by considering the crystal constitutive response as described in the next subsection.

3.2. Sensitivity constitutive problem

Through the crystal sensitivity constitutive sub-problem, the relationship between the crystal parameters, $\overset{\circ}{\boldsymbol{T}}$ and $\{\overset{\circ}{\boldsymbol{F}}, \overset{\circ}{\theta}\}$ is computed. As part of the update procedure, one computes the set $\{\overset{\circ}{\boldsymbol{T}}, \overset{\circ}{s}, \overset{\circ}{\tau}, \overset{\circ}{\boldsymbol{F}}^{\mathrm{e}}, \overset{\circ}{\boldsymbol{F}}^{\mathrm{p}}\}$ at each integration point in the microstructure at the end of the time increment t_{n+1}, where the sensitivity of the deformation gradient at the boundary of the microstructure $\overset{\circ}{\boldsymbol{F}}_{n+1}$ (and the sensitivity of the temperature field $\overset{\circ}{\theta}_{n+1}$) are known from the macro-perturbations. The microstructure configuration $\mathscr{B}_{n+1}$ is known at t_{n+1} from the direct problem. The constitutive sensitivity problem for a crystal orientation is history-dependent and the solution of the sensitivity problem at time t_n is known for each

crystal orientation, yielding the variables $\{\overset{\circ}{\boldsymbol{T}}, \overset{\circ}{s}, \overset{\circ}{\tau}, \overset{\circ}{\boldsymbol{F}}^{\mathrm{e}}, \overset{\circ}{\boldsymbol{F}}^{\mathrm{p}}\}$ at the beginning of each time increment. Although the microstructure interrogation problem is at a fixed temperature, the following discussion also includes thermal sensitivity effects based on $\overset{\circ}{\theta}_{n+1}$ from the macro-scale. Thermal effects would however play a role in multi-scale optimization (involving two scales of sensitivity problems) which would be a subject of future publication.

3.2.1. Computing the linear relation between $\overset{\circ}{s}^{\alpha}$ and $\{\overset{\circ}{\check{\boldsymbol{T}}}_{n+1}, \overset{\circ}{\theta}_{n+1}\}$

Consider the design-differentiation of the evolution equation for the deformation resistance, s^{α} (Eq. (29)). It results in:

$$\frac{\partial \overset{\circ}{s}^{\alpha}}{\partial t} = \sum_{\beta} \left[\overset{\circ}{h}^{\alpha\beta} |\dot{\gamma}^{\beta}| + h^{\alpha\beta} \, \overset{\circ}{|\dot{\gamma}^{\beta}|} \right]. \tag{48}$$

Incorporating Eqs. (30) and (31) and performing an Euler-backward integration results in:

$$\overset{\circ}{s}{}^{\alpha}_{n+1} - \Delta t \sum_{\beta} q^{\alpha\beta} \frac{\partial g^{\beta}}{\partial s^{\beta}} \overset{\circ}{s}{}^{\beta}_{n+1} = \overset{\circ}{s}{}^{\alpha}_{n} + \Delta t \sum_{\beta} q^{\alpha\beta} \frac{\partial g^{\beta}}{\partial \tau^{\beta}} \overset{\circ}{\tau}{}^{\beta}_{n+1} + \Delta t \sum_{\beta} q^{\alpha\beta} \frac{\partial g^{\beta}}{\partial \theta} \overset{\circ}{\theta}_{n+1}. \tag{49}$$

Solving the above set of equations for $\overset{\circ}{s}{}^{\alpha}_{n+1}$ results in:

$$\overset{\circ}{s}{}^{\alpha}_{n+1} = \sum_{\beta} m^{\alpha\beta} \overset{\circ}{\tau}{}^{\beta}_{n+1} + \upsilon_1^{\alpha} \overset{\circ}{\theta}_{n+1} + \upsilon_2^{\alpha}, \tag{50}$$

where $m^{\alpha\beta}$, υ_1^{α} and υ_2^{α} are constants. It is further known that $\tau^{\beta} = \check{\boldsymbol{T}} \bullet \boldsymbol{S}_0^{\alpha}$; design-differentiation of this relation results in $\overset{\circ}{\tau}{}^{\beta} = \overset{\circ}{\check{\boldsymbol{T}}} \bullet \boldsymbol{S}_0^{\alpha}$. Note that $\boldsymbol{S}_0^{\alpha}$ is a constant as it is expressed in the plastically deformed configuration which has the same crystal orientation as in the reference configuration. Substituting this relation into Eq. (50) results in the desired linear relation:

$$\left\{ \overset{\circ}{s}_{n+1} \right\} = \left[\frac{Ds}{D\tau} \right] : \overset{\circ}{\check{\boldsymbol{T}}} + \{\upsilon_1\} \overset{\circ}{\theta} + \{\upsilon_2\}, \tag{51}$$

where $\left[\frac{Ds}{D\tau}\right]$ is a third order tensor and υ_1, υ_2 are vectors.

3.2.2. Computing the linear relation between $\overset{\circ}{\boldsymbol{F}}^{\mathrm{p}}_{n+1}$ and $(\overset{\circ}{\check{\boldsymbol{T}}}_{n+1}, \overset{\circ}{\theta}_{n+1})$

The evolution equation for $\boldsymbol{F}^{\mathrm{p}}$ is evaluated, by design-differentiating Eq. (18), as:

$$\frac{\partial \overset{\circ}{\boldsymbol{F}}^{\mathrm{p}}}{\partial t} = \boldsymbol{L} \overset{\circ}{\boldsymbol{F}}^{\mathrm{p}} + \overset{\circ}{\boldsymbol{L}} \boldsymbol{F}^{\mathrm{p}}, \tag{52}$$

where $\overset{\circ}{\boldsymbol{L}} = \sum_{\alpha} [\overset{\circ}{\dot{\gamma}}{}^{\alpha} \boldsymbol{S}_0^{\alpha}]$ can be computed as

$$\overset{\circ}{\boldsymbol{L}} = \sum_{\alpha} \left[\frac{\partial \dot{\gamma}^{\alpha}}{\partial \tau^{\alpha}} \overset{\circ}{\tau}{}^{\alpha} + \frac{\partial \dot{\gamma}^{\alpha}}{\partial s^{\alpha}} \overset{\circ}{s}{}^{\alpha} + \frac{\partial \dot{\gamma}^{\alpha}}{\partial \theta} \overset{\circ}{\theta} \right] \boldsymbol{S}_0^{\alpha}. \tag{53}$$

Euler-backward integration of Eq. (52), with Eqs. (51), (53) and the earlier definition of $\overset{\circ}{\tau}{}^{\alpha}$ results in the following:

$$\overset{\circ}{\boldsymbol{F}}{}^{\mathrm{p}}_{n+1} (\boldsymbol{F}^{\mathrm{p}}_{n+1})^{-1} = \boldsymbol{E} + \mathscr{F} \left[\overset{\circ}{\check{\boldsymbol{T}}}_{n+1} \right] + \boldsymbol{G} \overset{\circ}{\theta}_{n+1}, \tag{54}$$

where $\underset{\circ}{\boldsymbol{E}}$, $\boldsymbol{G}$ are constant second-order tensors and $\mathscr{F}$ is a fourth-order tensor. Furthermore, $\overset{\circ}{\check{\boldsymbol{T}}}_{n+1}$ is related to $\overset{\circ}{\boldsymbol{F}}{}^{\mathrm{e}}_{n+1}$ and $\overset{\circ}{\theta}_{n+1}$ as (by design differentiating Eq. (24)):

$$\overset{\circ}{\check{\boldsymbol{T}}} = \left(\frac{\partial \mathscr{L}^{\mathrm{e}}}{\partial \theta}\right)\left[\check{\boldsymbol{E}}^{\mathrm{e}}\right]\overset{\circ}{\theta} + \mathscr{L}^{\mathrm{e}}\left[\mathrm{Sym}\left(\boldsymbol{F}^{\mathrm{e}\mathrm{T}}\overset{\circ}{\boldsymbol{F}}{}^{\mathrm{e}}\right)\right], \tag{55}$$

where $\mathscr{L}^{\mathrm{e}}$, the fourth-order anisotropic elasticity tensor, is assumed to be a function of temperature only. Using Eqs. (54) and (55), one can further obtain $\overset{\circ}{\boldsymbol{F}}{}^{\mathrm{p}}_{n+1}(\boldsymbol{F}^{\mathrm{p}}_{n+1})^{-1}$ as a function of $\overset{\circ}{\boldsymbol{F}}{}^{\mathrm{e}}_{n+1}$ and $\overset{\circ}{\theta}_{n+1}$.

3.2.3. Computing the linear relation between $\overset{\circ}{\boldsymbol{F}}{}^{\mathrm{e}}_{n+1}$ and $(\overset{\circ}{\boldsymbol{F}}_{n+1}, \overset{\circ}{\theta}_{n+1})$

Starting from the multiplicative decomposition of the deformation gradient, one can write $\overset{\circ}{\boldsymbol{F}}_{n+1} = \overset{\circ}{\boldsymbol{F}}{}^{\mathrm{e}}_{n+1}\boldsymbol{F}^{\mathrm{p}}_{n+1} + \boldsymbol{F}^{\mathrm{e}}_{n+1}\overset{\circ}{\boldsymbol{F}}{}^{\mathrm{p}}_{n+1}$, which can then be simplified to

$$(\boldsymbol{F}^{\mathrm{e}}_{n+1})^{-1}\left(\overset{\circ}{\boldsymbol{F}}_{n+1}\boldsymbol{F}^{-1}_{n+1}\right)\boldsymbol{F}^{\mathrm{e}}_{n+1} = (\boldsymbol{F}^{\mathrm{e}}_{n+1})^{-1}\overset{\circ}{\boldsymbol{F}}{}^{\mathrm{e}}_{n+1} + \overset{\circ}{\boldsymbol{F}}{}^{\mathrm{p}}_{n+1}(\boldsymbol{F}^{\mathrm{p}}_{n+1})^{-1}. \tag{56}$$

Substitution of the linear relationship between $\overset{\circ}{\boldsymbol{F}}{}^{\mathrm{p}}_{n+1}$ and $[\overset{\circ}{\boldsymbol{F}}{}^{\mathrm{e}}_{n+1}, \overset{\circ}{\theta}_{n+1}]$ results in the desired linear relationship:

$$\overset{\circ}{\boldsymbol{F}}{}^{\mathrm{e}}_{n+1} = \mathscr{C}'(\boldsymbol{V}_{n+1})\left[\overset{\circ}{\boldsymbol{F}}_{n+1}\right] + \boldsymbol{H}\left(\boldsymbol{V}_{n+1}, \overset{\circ}{\boldsymbol{V}}_{n}\right) + \boldsymbol{M}(\boldsymbol{V}_{n+1})\overset{\circ}{\theta}_{n+1}, \tag{57}$$

where $\boldsymbol{H}$ and $\boldsymbol{M}$ are known second-order tensor functions and $\mathscr{C}'$, a known fourth-order tensor function. The relationship between $\overset{\circ}{\boldsymbol{T}}_{n+1}$ and $[\overset{\circ}{\boldsymbol{F}}_{n+1}, \overset{\circ}{\theta}_{n+1}]$ is obtained by design differentiating Eq. (22):

$$\overset{\circ}{\boldsymbol{T}} = -\mathrm{tr}\left(\overset{\circ}{\boldsymbol{F}}{}^{\mathrm{e}}(\boldsymbol{F}^{\mathrm{e}})^{-1}\right)\boldsymbol{T} + \frac{1}{\det(\boldsymbol{F}^{\mathrm{e}})}\overset{\circ}{\boldsymbol{F}}{}^{\mathrm{e}}\check{\boldsymbol{T}}\boldsymbol{F}^{\mathrm{e}\mathrm{T}} + \frac{1}{\det(\boldsymbol{F}^{\mathrm{e}})}\boldsymbol{F}^{\mathrm{e}}\overset{\circ}{\check{\boldsymbol{T}}}\boldsymbol{F}^{\mathrm{e}\mathrm{T}} + \frac{1}{\det(\boldsymbol{F}^{\mathrm{e}})}\boldsymbol{F}^{\mathrm{e}}\check{\boldsymbol{T}}\overset{\circ}{\boldsymbol{F}}{}^{\mathrm{e}\,\mathrm{T}}. \tag{58}$$

Substitution of the linear relation between $\overset{\circ}{\boldsymbol{F}}{}^{\mathrm{e}}_{n+1}$ and $[\overset{\circ}{\boldsymbol{F}}_{n+1}, \overset{\circ}{\theta}_{n+1}]$ in Eq. (58) results in a linear relation between $\overset{\circ}{\boldsymbol{T}}_{n+1}$ and $[\overset{\circ}{\boldsymbol{F}}_{n+1}, \overset{\circ}{\theta}_{n+1}]$. This can be converted in terms of the PK I stress as

$$\overset{\circ}{\boldsymbol{P}} = \mathrm{tr}\left(\overset{\circ}{\boldsymbol{F}}_{n+1}\boldsymbol{F}^{-1}_{n+1}\right)\det\boldsymbol{F}_{n+1}\boldsymbol{T}\boldsymbol{F}^{-\mathrm{T}}_{n+1} + \det\boldsymbol{F}_{n+1}\overset{\circ}{\boldsymbol{T}}\boldsymbol{F}^{-\mathrm{T}}_{n+1} - \det\boldsymbol{F}_{n+1}\boldsymbol{T}\boldsymbol{F}^{-\mathrm{T}}_{n+1}\overset{\circ}{\boldsymbol{F}}{}^{T}_{n+1}\boldsymbol{F}^{-\mathrm{T}}_{n+1}. \tag{59}$$

From these equations, one can generate the constants in Eq. (47) and use this in the solution of the sensitivity kinematic problem.

3.3. Sensitivity of macro-properties

Finally, once the sensitivity micro-problem (Eq. (46)) is solved for stress sensitivities in the microstructure due to a perturbation in the process parameter (strain rates), the macro-stress sensitivities ($\frac{\partial \bar{\boldsymbol{T}}}{\partial \alpha_i}$) need to be calculated from Eq. (42) to drive the gradient optimization problem. This requires calculation of sensitivities of homogenized PK-1 stress using microstructure-average of the sensitivity fields using Eq. 43. This is followed by conversion of sensitivity of PK-1 stress to sensitivity of homogenized Cauchy stress using the homogenized counterpart of Eq. (59). Sensitivity of the equivalent stress is then evaluated as

$$\overset{\circ}{\bar{\sigma}}_{\text{eff}} = \frac{3}{2\bar{\sigma}_{\text{eff}}}\,\bar{\boldsymbol{T}}' \cdot \overset{\circ}{\bar{\boldsymbol{T}}}'. \tag{60}$$

The design examples as presented in the next section aim to control equivalent stresses over the deformation history of the material through design of strain rates ($\boldsymbol{\alpha}$). Gradients of the desired property $(\chi^i = \bar{\sigma}_{\text{eff}}(t = t_i),\ i = 1, \ldots, N_s)$ with respect to each process parameter α_j is then calculated using Eq. (42) and used in the gradient optimization algorithm which converges to an optimum value of the process parameter $\boldsymbol{\alpha}$ over a few iterations.

4. Numerical examples

In the numerical examples that follow, idealized grain structures are used to compare the performance of homogenization model vis-a-vis Taylor-based models in Example 1 and experimental results in Example 2. Interrogation of realistic 3D polyhedral microstructure is demonstrated in Example 3 followed by design examples where the equivalent stress history of complex 2D microstructures are controlled by designing the deformation strain rates in single (Example 4) and two-stage (Example 5) processes. A material composed of 99.987% pure polycrystalline FCC aluminum is used in these examples. The anisotropic elasticity tensor for FCC aluminum can be specified in terms of the three stiffness parameters (crystal stiffness tensor $\boldsymbol{C}$ in the crystal frame) which are approximated (in GPa) in terms of the temperature θ (in K) in Balasubramanian and Anand (2002) as follows:

$$\begin{aligned} c_{11} &= 123.323 + 6.7008 \times 10^{-8}\theta^3 - 1.1342 \times 10^{-4}\theta^2 - 7.8788 \times 10^{-3}\theta, \\ c_{12} &= 70.6512 + 4.4105 \times 10^{-8}\theta^3 - 7.5498 \times 10^{-5}\theta^2 + 3.9992 \times 10^{-3}\theta, \\ c_{44} &= 31.2071 + 7.0477 \times 10^{-9}\theta^3 - 1.2136 \times 10^{-5}\theta^2 - 8.3274 \times 10^{-3}\theta. \end{aligned} \tag{61}$$

Furthermore, the saturation values of the slip system resistances are taken equal for all slip systems as $s_s(300\ \text{K}) = 50.6$ MPa. Slip is assumed to occur in the twelve $111\langle 1\,1\,0\rangle$ slip systems. Additional material properties taken from Balasubramanian and Anand (2002) are listed in Table 1.

Example 1. Comparison of response of idealized 2D polycrystal in simple shear and plane strain compression with Taylor models.

Table 1
Material properties of FCC aluminum

Material parameter	Value
$\dot{\gamma}^0$	$1.732\text{E}+06\ \text{s}^{-1}$
h_0	250 MPa
r_1	2.0
p	0.141
q	1.1
$s_{\text{at},0}$	8.76 MPa
$s_{\text{t},0}$	8.76 MPa
ϖ	1.0
ρ	$2.77\ \text{Mg/m}^3$
c	920.0 J/kg K

The result of pure shear and plane strain compression of a 99.98% pure FCC aluminum aggregate using homogenization are compared with Taylor models based on stress–strain curves and texture evolution. The parameters used for the simulations are temperature of 300 K with strain rate of $6.667\text{E}-4\ \text{s}^{-1}$. Microstructure is modeled as a collection of 400 grains with each grain represented with a single finite element as shown in Fig. 2(a). The corresponding initial ODF is plotted in Fig. 2(d). The ODF is obtained by assuming that each orientation acts as a Gaussian point source within the fundamental region. This converts the discrete set of 400 orientations to a continuous distribution of orientations in the fundamental region. This representation was used in the ODF-Taylor simulation of Ganapathysubramanian and Zabaras (2005) for comparing with the FE-homogenized model. The reference fundamental region is discretized into 148 tetrahedral elements with cubic symmetry enforced in the solution procedure (for more details of this technique refer to Ganapathysubramanian and Zabaras (2005)). The ODF-Taylor method utilizes a finite element solution of ODF conservation law which conserves the crystal volume fractions over the polycrystal when grains reorient during deformation. The other model used for comparison is based on discrete-Taylor analysis of the aggregate of grains in Fig. 2(a). The constitutive law was calibrated with experimental results in Balasubramanian and Anand (2002) to suit Taylor based computations. Here, same constitutive law parameters are used for both Taylor model and FE homogenization. From Fig. 2(c) it can be seen that

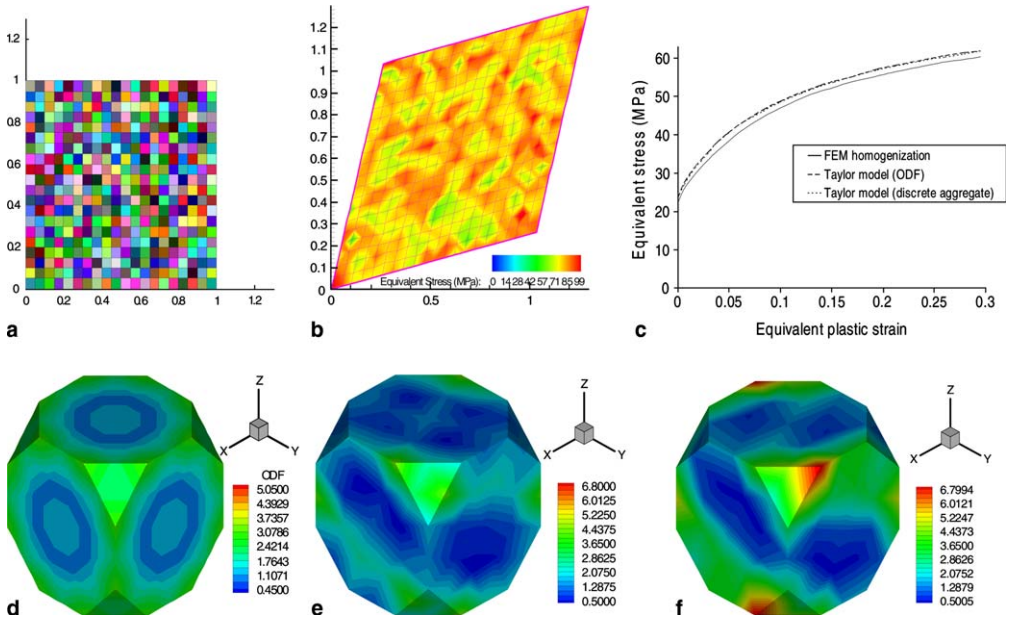

Fig. 2. Homogenization of an idealized 2D polycrystal: (a) Idealized 2D polycrystal with 400 grains with 1 finite element per grain. (b) Equivalent stress field after deformation in pure shear mode at a strain rate of $6.667\text{E}-4\ \text{s}^{-1}$. (c) Comparison of the equivalent stress–strain curve predicted through homogenization with Taylor simulation. (d) The initial texture of the polycrystals represented as an ODF in Rodrigues space. (e) Texture prediction using finite element homogenization and (f) texture prediction using the Taylor model at time $t = 210$ s. The Taylor model gives sharper and stronger textures and provides upper bound of the stress–strain curve.

homogenization technique provide a softer response than the Taylor model. The equivalent stress–strain curve obtained from ODF-Taylor and aggregate-Taylor almost exactly match. These models theoretically provide the upper bound of the stress–strain curve for the given microstructure due to strong kinematic constraint of equal deformation in all crystals. On the contrary, using finite element homogenization we find that crystal deformation is partitioned so that both compatibility and equilibrium are satisfied leading to a softer response. Uneven distribution of deformation among grains due to the effect of neighbors with various degrees of misorientation can be seen from the final microstructure in Fig. 4(a). Comparison of the ODFs in Figs. 2(e), (f) and 4(c), (d) show that Taylor model provides sharper textures as expected, while over-predicting the final texture. The $\langle 1\,1\,0\rangle$ and the $\langle 1\,1\,1\rangle$ pole figure from both the ODF-Taylor model and FE-homogenized model are further compared in shear (Fig. 3(a)) and plane strain compression (Fig. 3(b)) at equivalent strain of 0.3 reveal the sharper features of the Taylor model compared to FE-homogenization.

Example 2. Comparison of response of idealized 3D polycrystal in simple shear with experimental results from literature.

The experimental results of simple shear of an aggregate of FCC aluminum crystals were obtained by digitizing the stress–strain curves presented in Carreker and Hibbard (1957) (as was done in Balasubramanian and Anand (2002)). The experiment was performed at a constant strain rate of $6.667\text{E}-4\ \text{s}^{-1}$ and a temperature of 300 K. The numerical experiment simulated a simple shear motion with the final state of the microstructure depicted in Fig. 5(c). The initial texturing of the material is modelled to be random with the initial $\langle 1\,1\,0\rangle$ and $\langle 1\,1\,1\rangle$ pole figures shown in Fig. 5(b). A 512 grain idealized

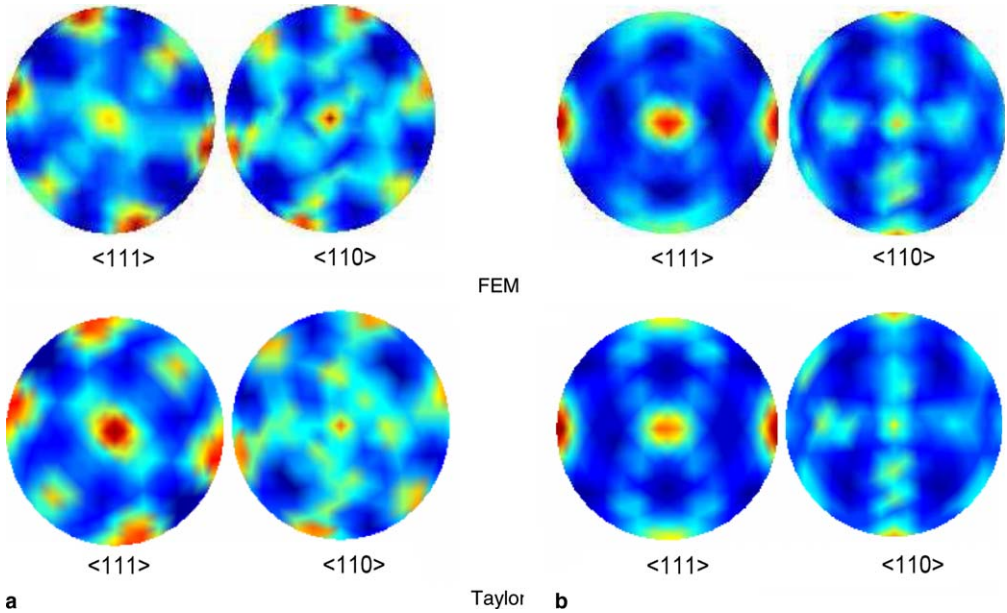

Fig. 3. Comparison of the FEM and Taylor predictions of final $\langle 1\,1\,0\rangle$ and $\langle 1\,1\,1\rangle$ textures after (a) pure shear and (b) plane strain compression.

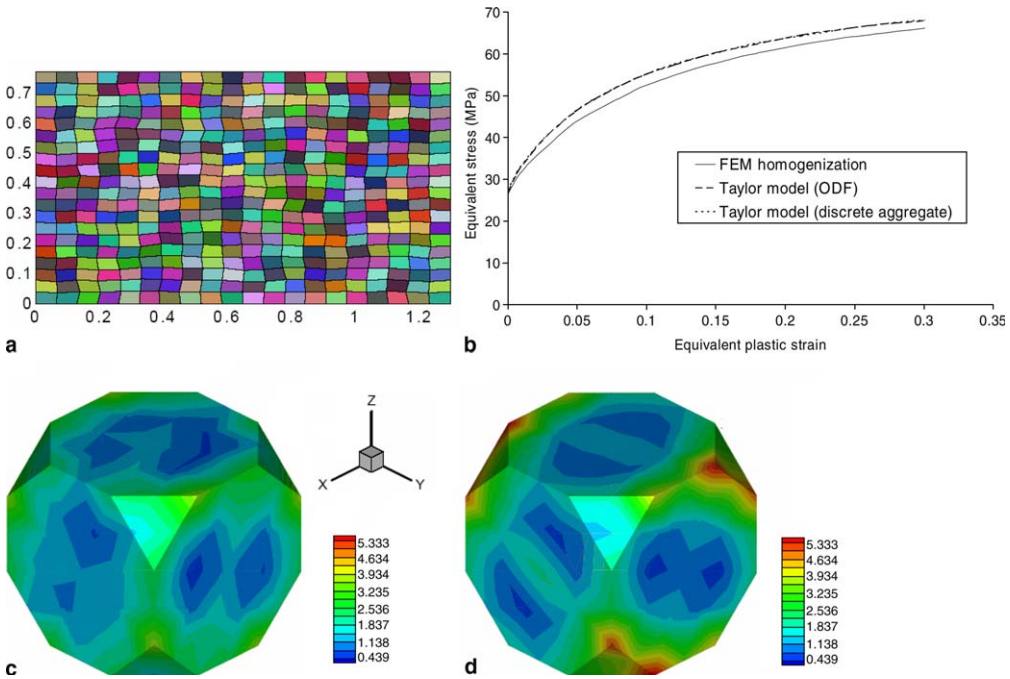

Fig. 4. (a) Final deformed state of the microstructure in Example 1 after plane strain compression. (b) Comparison of the equivalent stress–strain curve predicted through homogenization with Taylor simulation. (c) Texture prediction using finite element homogenization and (d) the Taylor model at $t = 130$ s.

microstructure (with 1 finite element per grain) is used in the homogenization procedure to numerically generate the response to simple shear. The predicted and experimental stress–strain responses are superposed in Fig. 5(d). The simulation was also carried out using the the 400 grain 2D idealized microstructure in Example 1 using an initial random texture and the corresponding stress–strain curve is also superposed in Fig. 5(d) showing that a 2D approximation is equally valid in this case. Numerical response closely follows the experimental response but is softer since parameters calibrated using Taylor model (in Balasubramanian and Anand (2002)) were used in the homogenization model. The final texture of the material represented using the $\langle 1\,1\,0\rangle$ and $\langle 1\,1\,1\rangle$ pole figures are also depicted in Fig. 5(b). As expected, simulated texture is dominated by x-axis $\langle 1\,1\,0\rangle$ fibers, (along the x-face of the ODF) at the strain level of 0.3, as seen from the final ODF obtained in Fig. 5(a).

Example 3. Response of realistic 3D microstructures.

Example of interrogation of realistic 3D microstructures obtained from Monte Carlo Potts grain growth program from the work in Sundararaghavan and Zabaras (2005a) is demonstrated in Fig. 6. Finite element discretization of the 3D microstructure was directly transferred from the structured mesh used in the Monte Carlo Potts simulation. The domain is discretized using a $24 \times 24 \times 24$ grid and is shown in Fig. 6. The homogenized response of the microstructure in plane strain compression and shear is compared and presented in Fig. 6(b). The equivalent stress field for both shear and plane strain compression

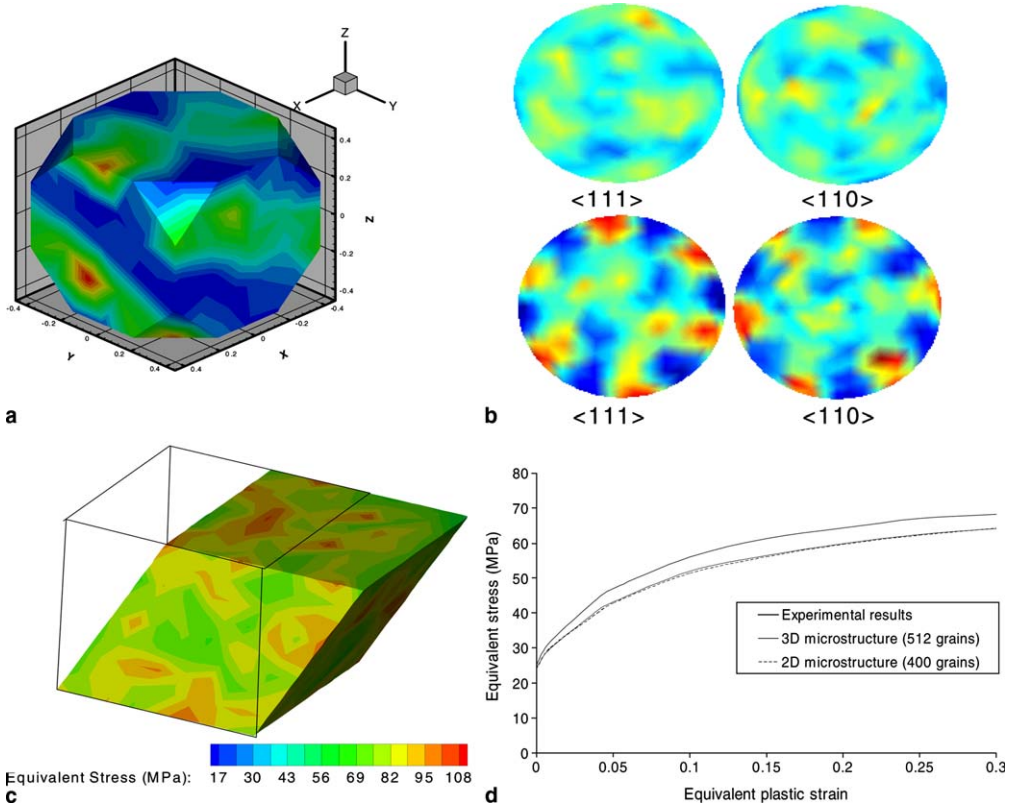

Fig. 5. Homogenization of an idealized 3D polycrystal with 512 grains: (a) The final ODF obtained after simple shear. (b) The initial random texture of the material (top) represented using the ⟨1 1 0⟩ and ⟨1 1 1⟩ pole figures. The final pole figures after deformation are shown at the bottom (c) Equivalent stress field after deformation in pure shear mode. (d) Comparison of the equivalent stress–strain curve predicted through homogenization with experimental results from Carreker and Hibbard (1957).

is compared at a homogenized strain level of 0.060 in Figs. 6(c) and (d), respectively. The simulation was performed on 60 X64 Intel processors with a clock speed of 3.6 GHz using PetSc KSP solvers on the Cornell theory center's supercomputing facility. Each simulation was carried out over 2000 equal time steps and took about 1200 min to solve in the parallel environment.

Example 4. Design for desired plastic response under a combination of process modes.

Two 2D microstructures (Figs. 7(a) and (b)) (from now on referred to as microstructures A and B, respectively) with 151 and 162 grains, respectively, generated using a standard voronoi construction and meshed using OOF-2 is employed in the design examples. Microstructure A is meshed using 3989 quadrilateral elements and microstructure B is meshed using 4200 quadrilateral elements. The mesh conforms to grain boundaries such that each element is fully within a particular grain. An initial random ODF is assigned to these microstructures as shown in the pole figures in Figs. 7(c) and (d) corresponding to microstructures A and B, respectively. Aim of this example is to demonstrate the technique for

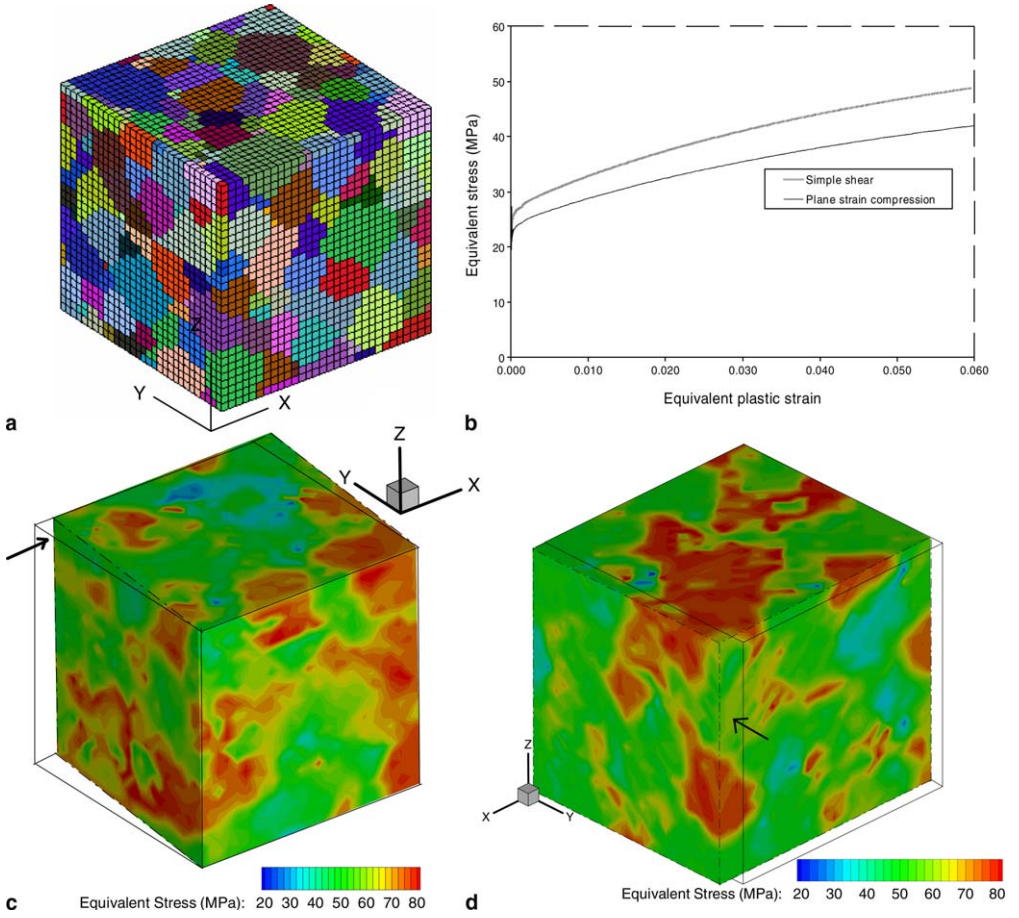

Fig. 6. (a) Microstructure obtained from a MC grain growth simulation (b) Comparison of equivalent stress–strain curve for the two cases and equivalent stress field of a 3D microstructure (above) after (c) simple shear and (d) plane strain compression.

obtaining desired equivalent stress response in microstructure A by controlling a combination of process modes applied on the microstructure. Sensitivities are computed with a perturbation of $\Delta\boldsymbol{\alpha}_i = 1\mathrm{E}-5$ for each process mode i. Thus, optimization is comprised of one direct and three sensitivity problems. The optimization problem is executed until the objective function becomes less than $1\mathrm{E}-3$ or if the objective function normalized with the initial objective showed less than $1\mathrm{E}-4$ improvement between iterations. The response is computed for a total time of 11 s with a total of 200 time steps.

The desired response is shown in Fig. 8(a) and is assumed to occur during a single processing stage with unknown velocity gradient. Through optimization, we desire to identify the velocity gradient applied on the microstructure. The desired response for the microstructure under consideration is assumed to be a simple cubic curve with equivalent stress vs time characteristics of 30 MPa at 0.5 s, 40 MPa at 3 s, 47.5 MPa at 7 s, and 55 MPa at 11 s of deformation as shown in Fig. 8(a). Initial guess strain rate of $5\mathrm{E}-4$ is given to all three process modes of shear, rotation and plane strain compression, i.e. a vector of

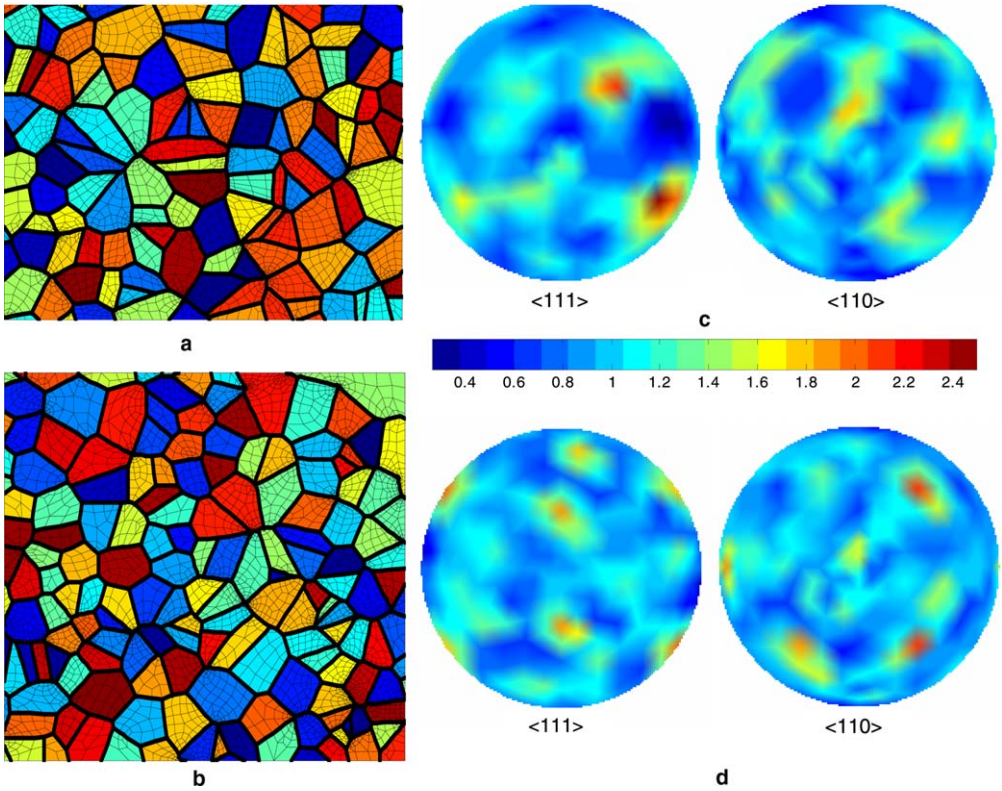

Fig. 7. Initial microstructure for the design problems. (a) Microstructure A with 151 grains, (b) microstructure B with 162 grains. Initial random texture depicted using the $\langle 1\,1\,0\rangle$ and $\langle 1\,1\,1\rangle$ pole figures for microstructure A in (c) and microstructure B in (d).

$\boldsymbol{\alpha} = [5\mathrm{e}-4, 5\mathrm{e}-4, 5\mathrm{e}-4]$ is used in the first iteration. The response obtained in the first iteration, two intermediate iterations and the final iteration are shown in Fig. 8(b). The desired response is obtained with a converged mean square error (Eq. (41)) of 0.51 and final parameters are found as $\boldsymbol{\alpha} = [1.66\mathrm{E}-3, 8.42\mathrm{E}-3, 5\mathrm{E}-4]$. Fig. 8(d) shows rapid convergence of the objective function with increasing number of iterations showing the numerical efficiency of the algorithm. Final microstructure at a time of 11 s is shown in Fig. 8(c). Initially each grain was assigned a unique orientation. During deformation, misorientation develops within grains leading to spread of orientations and development of strong intra-granular texture. The misorientation development can be visualized using the change in neo-eulerian angle of rotation $\xi(t)$ at time t from the values of $\xi(t=0)$ of the initial texture. ξ is obtained from the Rodrigues parametrization given by $\boldsymbol{r} = \boldsymbol{n}\tan(\frac{\xi}{2})$ where $\boldsymbol{n}$ denotes the axis of rotation. The change in the neo-Eulerian angle from the initially assigned orientation of grains shown in Fig. 8(c) clearly shows the formation of disoriented regions within grains at moderate deformation.

Example 5. Design of desired second stage microstructure response in two-stage processes with unloading and development of residual stresses.

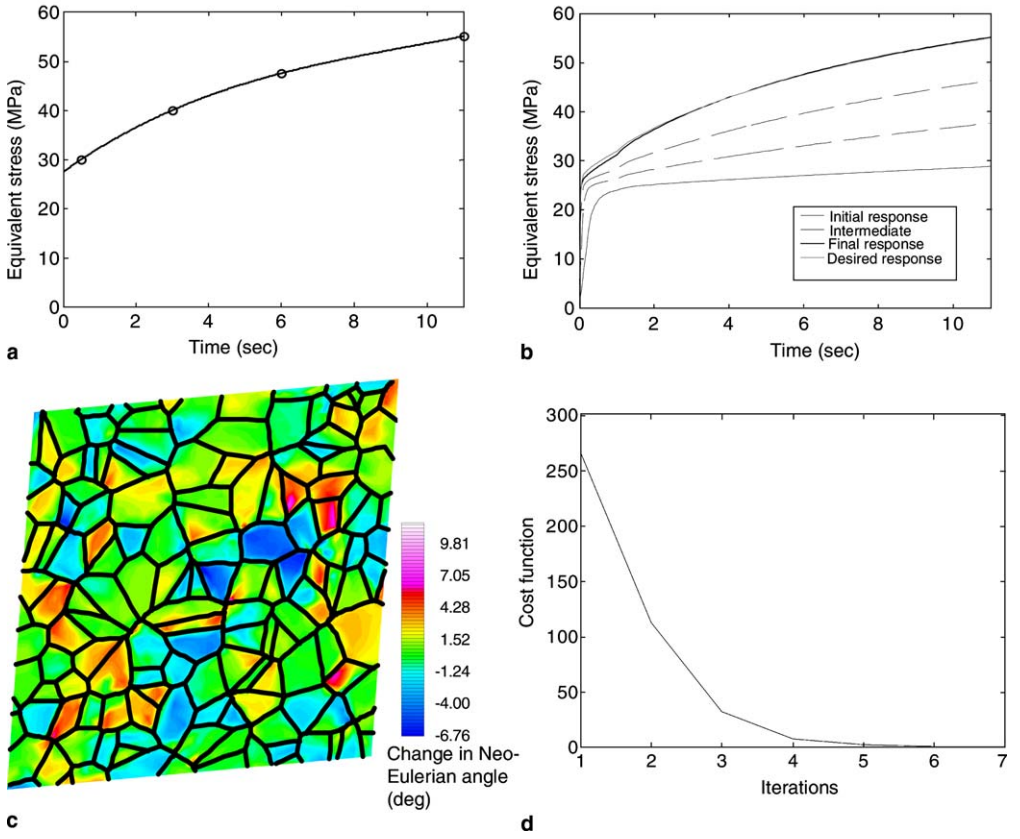

Fig. 8. Design for desired material response. (a) Desired response of the material given by a smooth cubic interpolation of four desired coordinates. (b) Change in the microstructure response over various iterations of the optimization problem. (c) Final microstructure at time $t = 11$ s of the design solution with mis-orientation distribution over grains. (d) Change in objective function over various design iterations of gradient minimization algorithm.

The same model can be extended towards control in a multi-stage set up where a sequence of process modes can be designed to achieve desired response in the processed microstructure. A crucial aspect in multi-stage simulation is an accurate model of mechanics in-between stages. This phase consists of removal of loads from the microstructure and development of residual stresses. The unloading process here is modelled as a non-linear (finite deformation) elasto-static boundary value problem. If $\mathscr{B}$ represents the final configuration of the workpiece at the end of the loading phase with the total deformation gradient given as $\boldsymbol{F}_{n+1} = \boldsymbol{F}^{\mathrm{e}}\boldsymbol{F}^{\mathrm{p}}$, then the solution to the unloading process results in the final body configuration $(\mathscr{B}_u)$ with the total deformation gradient after unloading given as $\boldsymbol{F}_u = \boldsymbol{F}^{\mathrm{e}}_u\boldsymbol{F}^{\mathrm{p}}$. In this work, two assumptions are made to model unloading: firstly, no crystal reorientation is assumed to occur on unloading and secondly, no recovery (or evolution of state) is assumed to occur. Microstructure proceeds from one stage to another stage immediately upon completion of the unloading process. For design problems involving the unloading stage, we need to consider the sensitivity of a finite deformation elasto-static problem. The sensitivity constitutive problem is modified and the material deformation

behavior treated as elastic in the unloading phase. During the unloading process, we assume for simplicity that the bottom edge of the microstructure is fixed to prevent motion in the normal direction.

Microstructure B is used in this example. A perturbation of $1E-5$ is applied to the strain rate in the first stage. Sensitivity of residual stresses after unloading in the first stage are transferred to the second stage. Aim of this example is to demonstrate the technique for obtaining desired initial microstructure response after unloading from a process by controlling the strain rate of initial loading. Unloading produces a heterogeneous distribution of residual stresses in the microstructure. High residual stresses are displayed by grains in the vicinity of grains that displayed high stresses at the end of first stage as seen by comparing residual stress distribution in Fig. 9(e) and the final stress state at the end of first stage in Fig. 9(d). The second stage response is not only affected by the heterogeneity of residual stresses but also due to changes in texture and slip system resistance (state variable) distribution at the start of second stage. By controlling the strain rates used in the first stage, parameters such as initial texturing and state variable at the start of the second stage are also controlled. Numerical experiments reveal that the state variable distribution at the end of the first stage is a dominant factor in determining the material response at the second stage. Response shown in Fig. 9(a) corresponds to the desired equivalent stress-time curve in the second stage under plane strain compression of the microstructure at a strain rate of $5E-3$ mm/s. The velocity gradient applied to the microstructure in the

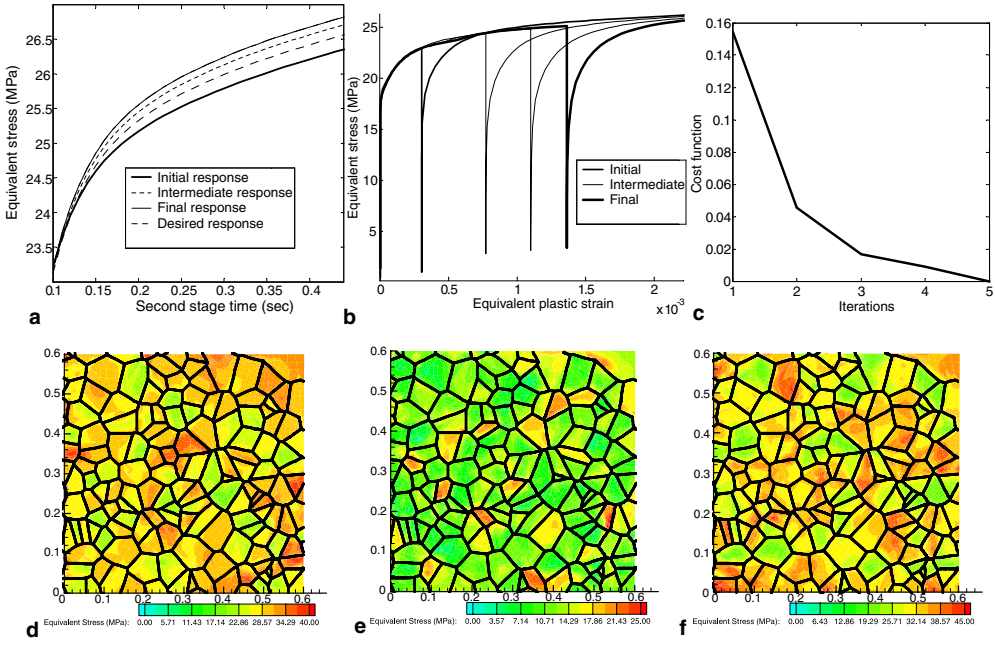

Fig. 9. (a) Desired response in the second stage and response obtained at various design iterations. (b) Microstructure response in the first deformation stage at various design iterations. (c) Change in objective function over various design iterations of gradient minimization algorithm. (d) Equivalent stress distribution (at final design solution) at the end of first deformation stage (time $t = 1$ s). (e) Residual equivalent stress distribution after unloading at the end of first stage. (f) Equivalent stress distribution at the microstructure at time $t = 0.45$ s of the second stage (plane strain compression).

first stage (simple shear) is unknown and is taken as the design variable. Initial guess strain rate of $5E-4\,s^{-1}$ is given to the first stage, i.e. a vector of $\boldsymbol{\alpha} = [0, 5e-4, 5e-4]$ is employed. After optimization, the optimal first loading stage strain rates were found as $\boldsymbol{\alpha} = [0, 1.442E-3, 1.442E-3]$ resulting in a response which was within a mean square error of $1E-6$ from the desired response. Equivalent stress field of the microstructure before and after unloading (initial state for the second stage) and after 0.45 s of second stage are presented in Figs. 9(d), (e) and (f), respectively. Figs. 9(a) and (b) show evolution of the response at various iterations of the optimization algorithm and Fig. 9(c) shows rapid convergence of the objective function with increasing number of iterations again demonstrating the numerical efficiency of the design algorithm.

5. Conclusions and future work

A finite element homogenization model is presented for modelling elasto-viscoplastic behavior and texture evolution in a polycrystal subject to finite strains. The technique utilizes macro-micro linking techniques obtained from homogenization theory. An updated Lagrangian finite element formulation is invoked to interrogate the microstructure and averaging schemes are utilized to identify the macro-response. The model is found to be capable of predicting non-homogeneous stress and deformation fields in 2D and 3D microstructures. Comparison to ODF-Taylor, aggregate-Taylor and experimental results with respect to the equivalent stress–strain curves and texture development reveals that the model performs as expected providing softer response and smoother textures. The problem of microstructure design is then attempted using a novel continuum sensitivity analysis of homogenization. This involves differentiation of the governing field equations of homogenization with respect to the processing parameters and development of the weak forms for the corresponding sensitivity equations that are solved using finite element analysis. The technique is applied to identify optimal strain rates in single and multi-stage processes (with intermediate unloading stages) that would lead to a desired microstructure response. The algorithm is computationally efficient and is found to converge to the desired response within a few iterations.

Work presented here is focused on the material point problem of controlling microstructures to obtain desired response. Few issues in design are still to be addressed, firstly a question of how to select an appropriate sequence of processes for increasing the likelihood of achieving a desired response. Secondly, explore the applicability of controlling the initial features (texture and misorientations) of the microstructure to obtain desired response. We plan to address these problems using statistical learning techniques such as those proposed by the authors recently in Sundararaghavan and Zabaras (2005a). Another area will be to develop gradient optimization techniques for microstructure-sensitive design of thermo-mechanical forming processes. In the future, the present analysis will be linked to a continuum model and CSM-based techniques will be extended in a multiscale framework to control macro-parameters (entities like preform and die shapes) to achieve desired properties.

Acknowledgements

The work presented here was funded by the Mechanical Behavior of Materials program (Dr. D. Stepp, program manager) of the Army Research Office (Grant W911NF-04-1-0283)

and by the Computational Mathematics program (Dr. F. Fahroo, program manager) of the Air Force Office of Scientific Research (Grant FA9550-04-1-0070). The work was conducted using the super-computing facilities of the Cornell Theory Center.

References

Adams, B.L., Henrie, A., Henrie, B., Lyon, M., Kalidindi, S.R., Garmestani, H., 2001. Microstructure sensitive design of a compliant beam. J. Mech. Phys. Solids 49, 1639–1663.

Acharjee, S., Zabaras, N., 2003. A proper orthogonal decomposition approach to microstructure model reduction in Rodrigues space with applications to the control of material properties. Acta Mater. 51/18, 5627–5646.

Akkaram, S., Zabaras, N., 2001. An updated Lagrangian finite element sensitivity analysis of large deformations using quadrilateral elements. Int. J. Numer. Meth. Eng. 52, 1131–1163.

Balasubramanian, S., Anand, L., 2002. Elasto-viscoplastic constitutive equations for polycrystalline fcc materials at low homologous temperatures. J. Mech. Phys. Solids 50, 101–126.

Beaudoin, A.J., Mecking, H., Kocks, U.F., 1996. Development of localized orientation gradients in fcc polycrystals. Philos. Mag. A 73, 1503–1518.

Becker, R., Panchanadeeswaran, S., 1995. Effects of grain interactions on deformation and local texture in polycrystals. Acta Metall. Mater. 43, 2701–2719.

Bronkhorst, C.A., Kalidindi, S.R., Anand, L., 1992. Polycrystalline plasticity and the evolution of crystallographic texture in fcc metals. Philos. Trans. R. Soc. Lond. A 341, 443–477.

Carreker, R., Hibbard, W., 1957. Tensile deformation of aluminum as a function of temperature, strain rate and grain size. Trans. AIME 209, 1157–1163.

Diard, O., Leclercq, S., Rousselier, G., Cailletaud, G., 2005. Evaluation of finite element based analysis of 3D multicrystalline aggregates plasticity: application to crystal plasticity model identification and the study of stress and strain fields near grain boundaries. Int. J. Plasticity 21 (4), 691–722.

Ganapathysubramanian, S., Zabaras, N., 2004. Design across length scales: a reduced-order model of polycrystal plasticity for the control of microstructure-sensitive material properties. Comput. Meth. Appl. Mech. Eng. 193 (45–47), 5017–5034.

Ganapathysubramanian, S., Zabaras, N., 2005. Modeling the thermoelastic-viscoplastic response of polycrystals using a continuum representation over the orientation space. Int. J. Plasticity 21/1, 119–144.

Gurson, A., 1977. Continuum theory of ductile rupture by void nucleation and growth: Part I: yield criteria and flow rules for porous ductile media. J. Eng. Mater. Technol. 99, 2–15.

Gurtin, M.E., 1981. An Introduction to Continuum MechanicsMathematics in Science and Engineering, vol. 158. Academic Press, New York.

Harren, S.V., Asaro, R.J., 1989. Nonuniform deformations in polycrystals and aspects of the validity of the Taylor model. J. Mech. Phys. Solids 37, 191–232.

Havner, K.S., 1992. Finite plastic deformation of crystalline solids. Cambridge Monographs on Mechanics and Applied Mathematics. Cambridge University Press, Cambridge.

Hill, R., 1952. The elastic behavior of a crystalline aggregate. Proc. Phys. Soc. Lond. A 65, 349–354.

Hill, R., 1965. Continuum micro-mechanics of elastoplastic polycrystals. J. Mech. Phys. Solids 13, 89–101.

Hill, R., 1972. On constitutive macro-variables for heterogeneous solids at finite strain. Proc. Roy. Soc. Lond. A 326, 131–147.

Hill, R., 1984. On macroscopic effects of heterogeneity in elastoplastic media at finite strain. Math. Proc. Camb. Philos. Soc. 95, 481–494.

Kocks, U.F., Tóme, C.N., Wenk, H.R., 1998. Texture and Anisotropy: Preferred Orientations in Polycrystals and their Effect on Materials Properties. Cambridge University Press, Cambridge.

Kothari, M., Anand, L., 1998. Elasto-viscoplastic constitutive equations for polycrystalline metals: application to tantalum. J. Mech. Phys. Solids 46, 51–83.

Matous, K., Maniatty, A.M., 2004. Finite element formulation for modelling large deformations in elasto-viscoplastic polycrystals. Int. J. Numer. Meth. Eng. 60, 2313–2333.

Miehe, C., Schröder, J., Schotte, J., 1999. Computational homogenization analysis in finite plasticity simulation of texture development in polycrystalline materials. Comput. Meth. Appl. Mech. Eng. 171, 87–418.

Mika, D.P., Dawson, P.R., 1999. Polycrystal plasticity modeling of intracrystalline boundary textures. Acta Mater. 47, 1355–1369.

Nemat-Nasser, S., 1999. Averaging theorems in finite deformation plasticity. Mech. Mater. 31, 493–523.
Nemat-Nasser, S., Hori, M., 1993. Micromechanics: Overall Properties of Heterogeneous Solids. Elsevier, Amsterdam.
OOF-2, Object oriented finite element analysis of real material microstructures, NIST Public domain software available at http://www.ctcms.nist.gov/oof/oof2.html.
Sarma, G.B., Radhakrishnan, B., Dawson, P.R., 2002. Mesoscale modeling of microstructure and texture evolution during deformation processing of metals. Adv. Eng. Mater. 4, 509–514.
Sundararaghavan, V., Zabaras, N., 2005a. On the synergy between texture classification and deformation process sequence selection for the control of texture-dependent properties. Acta Mater. 53, 1015–1027.
Sundararaghavan, V., Zabaras, N., 2005b. Classification of three-dimensional microstructures using support vector machines. Comput. Mater. Sci. 32, 223–239.
van der Sluis, O., Schreurs, P.J.G., Brekelmans, W.A.M., Meijer, H.E.H., 2000. Overall behaviour of heterogeneous elasto-viscoplastic materials: effect of microstructural modeling. Mech. Mater. 32, 449–462.